Statistics of cosmological Lyman α absorption

Article (Published Version)

Monthly Notices
of the
ROYAL ASTRONOMICAL SOCIETY

Mon. Not. R. Astron. Soc. **427,** 2359–2375 (2012) doi:10.1111/j.1365-2966.2012.22136.x

Statistics of cosmological Lyman α absorption

Dipak Munshi,[1]⋆ Peter Coles[1] and Matteo Viel[2,3]

[1]*School of Physics and Astronomy, Cardiff University, Queen's Buildings, 5 The Parade, Cardiff, CF24 3AA*
[2]*INAF-Observatorio Astronomico di Trieste, Via G.B. Tiepolo 11, I-34131, Trieste, Italy*
[3]*INFN sez. Trieste, via Valerio 2, 34127, Trieste, Italy*

Accepted 2012 September 13. Received 2012 September 11; in original form 2011 December 21

ABSTRACT

We study the effect of the non-Gaussianity induced by gravitational evolution upon the statistical properties of absorption in quasar (quasi-stellar object) spectra. Using the generic hierarchical ansatz and the lognormal approximation, we derive the analytical expressions for the one-point probability distribution function (PDF) as well as for the joint two-point PDF of transmitted fluxes in two neighbouring quasi-stellar objects. These flux PDFs are constructed in three dimensions as well as in projection (i.e. in two dimensions). The PDFs are constructed by relating the lower-order moments (i.e. cumulants and cumulant correlators) of the fluxes to the three-dimensional neutral hydrogen distribution, which is, in turn, expressed as a function of the underlying dark matter distribution. Next, the lower-order moments are modelled using a generating function formalism in the context of a minimal tree-model for the higher-order correlation hierarchy. These different approximations give nearly identical results for the range of redshifts probed, and we also find very good agreement between our predictions and the outputs of hydrodynamical simulations. The formalism developed here for the joint statistics of flux-decrements concerning two lines of sight can be extended to multiple lines of sight, which could be particularly important for the three-dimensional reconstruction of the cosmic web from the spectra of quasi-stellar objects (e.g. in the Baryon Oscillation Spectroscopic Survey). These statistics probe the underlying projected neutral hydrogen field and are thus linked to hotspots of absorption. The results for the PDF and the bias presented here use the same functional forms of scaling functions that have previously been employed for the modelling of other cosmological observations, such as the Sunyaev–Zel'dovich effect.

Key words: cosmology: theory – large-scale structure of Universe.

1 INTRODUCTION

Ongoing cosmic microwave background (CMB) experiments such as *Planck*,[1] the Atcama Cosmology Telescope[2] (ACT) and the South Pole Telescope[3] (SPT) aim to pinpoint the cosmological parameters that describe the background geometry and dynamics of the Universe in unprecedented detail. Along with very precise constraints on the structure of the Universe on the largest scales, smaller-scale observables will be crucial in order to further constrain the cosmological concordance model or to find possible deviations from it. In particular, galaxy clustering surveys, such as the Baryon Oscillation Spectroscopic Survey (BOSS) and the Six-degree-Field Galaxy Survey (6dF), and future weak lensing and clustering observations (e.g. *EUCLID*) could probe smaller scales and new redshift regimes. Spectroscopic surveys, such as BOSS[4] (and BigBOSS) will also trace the large-scale distribution of the baryonic matter in the Universe through the study of the flux distribution of Lyman α absorption systems in a very large number of quasar [quasi-stellar object (QSO)] spectra.

The Lyman α forest (i.e. the many absorption features in QSO spectra), which is produced by intervening neutral hydrogen in the intergalactic medium (IGM) along the line of sight, is well known as an important cosmological probe (for a recent review, see Meiksin 2010). In the standard cosmological paradigm, the IGM consists of mildly non-linear gas, making up the cosmic web, that traces the dark matter

⋆E-mail: Dipak.Munshi@astro.cf.ac.uk
[1] http://www.rssd.esa.int/Planck
[2] http://www.physics.princeton.edu/act/
[3] http://pole.uchicago.edu/
[4] http://cosmology.lbl.gov/BOSS/

and is photoheated by an ultraviolet (UV) background. Thus, the Lyman α forest is the main probe of the IGM, and it has been shown to arise naturally in hierarchical structure formation scenarios. Astrophysical effects produced by feedback from galaxies and/or active galactic nuclei (AGNs) do not seem to strongly affect the vast majority of the baryons in the cosmic web (Theuns et al. 2002a; McDonald et al. 2005), thereby this can be used as a dark matter tracer. The relation between the Lyman α forest flux and the underlying matter field is a non-linear one and it is generally expected that statistics of Lyman α are biased relative to the underlying dark matter distribution. The Lyman α forest has been studied using a variety of analytical techniques, such as the Zel'dovich approximation, which is valid in the quasi-linear regime and is often used in modelling of non-linear gravitational clustering (Zel'dovich 1970; Doroshkevich & Shandarin 1977; McGill 1990; Hui, Gnedin & Zhang 1997; Matarrese & Mohayee 2002). In addition, the lognormal approximation (Coles & Jones 1991) is frequently used to model the statistics of the Lyman α forest (Bi 1993; Gnedin & Hui 1996; Bi & Davidson 1997; Roy Choudhury, Padamanabhan & Srianand 2001; Viel et al. 2002). Models based on the hierarchical or scaling ansatz (Balian & Schaeffer 1989; Bernardeau & Schaeffer 1992, 1999) for higher-order correlation functions have also been investigated in order to model the statistics of the Lyman α forest (Valageas, Schaeffer & Silk 1999).

In addition to analytical modelling, hydrodynamical simulations have also played a very important role in this field (e.g. Cen et al. 1994; Croft et al. 1998, 1999; Gnedin & Hui 1998; Meiksin & White 2001) and support the simple analytical picture. Thus, analytical schemes, including the ones that we develop here, can be calibrated using numerical simulations, which, in turn, allows us to explore a large parameter space efficiently. However, numerical simulations are required to resolve the Jeans scale of the photoionized warm IGM, and this requirement typically means small box sizes that sample larger-scale modes rather poorly. Indeed, several seminumerical prescriptions, which are not entirely based on hydrodynamical simulations, have also been developed to model Lyman α flux and to recover the correlation function from observed data sets (Slosar et al. 2011).

The two most commonly used approaches in Lyman α studies are based either on decomposing the information encoded in the transmitted flux via Voigt profile fitting or treating the flux as a continuous field.

In the first approach, the shapes and clustering properties of absorption lines fitted by Voigt profiles have been investigated in a variety of studies involving the temperature of the IGM (Schaye et al. 1999; McDonald et al. 2001), in order to constrain the reionization history (Rauch et al. 1997; Theuns et al. 2002b; Hui & Haiman 2003), to measure the matter power spectrum and cosmological parameters (Croft et al. 1999; McDonald & Miralda-Escudé 1999; Rollinde et al. 2003; Viel, Haenelt & Springel 2004b; Coppolani et al. 2006; McDonald, Seljak & Burles 2006; Viel & Haehnelt 2006; Guimarães et al. 2007).

By using the second set of methods, the statistical properties of the flux, such as the mean flux level, flux probability distribution function (PDF), flux power spectrum (Viel et al. 2004b, 2008; Seljak, Slosar & McDonald 2006) and flux bispectrum, are typically employed to explore flux statistics. For example, it has been shown that the mean-flux level can be used to constrain the amplitude of intergalactic UV background (Tytler et al. 2004; Bolton et al. 2005) while the flux PDF (Bolton, Oh & Furlanetto 2009; McQuinn et al. 2009) is sensitive to the thermal evolution of the IGM (see also Lidz et al. 2006). However, the flux power spectrum can be used to constrain the cosmological parameters and the nature of dark matter (Croft et al. 2002). The flux bispectrum (Viel et al. 2009a) contains useful information about the primordial, as well as gravity-induced (i.e. secondary), non-Gaussianity. The data typically used in these investigations consist mainly of two different sets of QSO spectra: the Sloan Digital Sky Survey (SDSS) low-resolution low-signal-to-noise spectra and the Ultraviolet and Visual Echelle Spectrograph (UVES)/Very Large Telescope (VLT) or High Resolution Echelle Spectrometer (HIRES)/KECK high-resolution spectra. The number of SDSS spectra is about a factor of $\sim$200 larger than that of high-resolution samples, although the latter probe the smaller scales with greater accuracy.

More recently, it has been argued that BOSS-like QSO spectroscopic surveys could detect baryon acoustic oscillation (BAO) signatures at high redshift (McDonald & Eisenstein 2007) and that a sample of QSO pairs could constrain the geometry of the high-redshift universe (McDonald 2003). Furthermore, an analysis of coincident absorption lines in QSO pairs can also allow departures from the Hubble flow and allow non-gravitational effects to be measured (Rauch et al. 2005).

The SDSS-III/BOSS aims to identify and observe more than 160 000 QSOs over $\sim$10 000 deg^2 within a redshift range $z = (2.15–3.5)$; for more details, see Eisenstein et al. (2011) and Ross et al. (2012). This survey is primarily design to study BAOs by performing a full three-dimensional (3D) sampling of the matter density. Such studies will also provide an unprecedented opportunity to study the clustering statistics using projected Lyman α flux decrements of QSOs.

In this paper, we consider the Lyman α flux decrement in two dimensions, which is related to the projected density of neutral hydrogen. The statistical study of projected Lyman α flux decrement can be performed using one- or two-point PDFs or their lower-order moments. The PDFs contain information of cumulants or their correlators to an arbitrary order and can be constructed using the well-established machinery of a hierarchical ansatz (Munshi, Coles & Melott 1999a,b; Munshi, Melott & Coles 2000). Several authors have recently studied the lower-order cumulants of Lyman α forests and cross-correlated them against weak lensing convergence as well as the CMB sky (Vallinotto et al. 2009; Valentino et al. 2011). The results presented here are complementary to such studies because we take into account the lower-order moments to an arbitrary order, not just for the one-point cumulants but also for their two-point counterparts or cumulant correlators. The cumulant correlators are the two-point analogues of one-point cumulants and they are already in use in different areas of cosmology, such as in the analysis of galaxy surveys (Szapudi & Szalay 1999). The lowest in the two-point hierarchy is the two-point correlation function. In the context of Lyman α studies, the two-point correlation function has already been introduced in studies involving two neighbouring line of sights (D'Odorico, Petitjean & Cristiani 2002; Viel et al. 2002). Our study generalizes these results to probe non-Gaussian correlation functions involving multiple lines of sight. We model the statistics of underlying neutral hydrogen distribution using a lognormal distribution

as well as an extension of the perturbation theory approach (Valageas & Munshi 2004) in three dimensions. Predictions from these models are then tested using hydrodynamical simulations at three different redshifts ($z = 2$, 3 and 4). Next, we use these results to build and test a statistical description of the projected flux distribution. The results presented here can be generalized to cross-correlation studies involving external data sets and Lyman α flux distribution. The correlation functions are equivalent to their Fourier (harmonic) space counterpart, the multispectra, recently introduced by Munshi & Heavens (2010).

The plan of this paper is as follows. In Section 2, we introduce the notations and define the relevant quantities, such as the transmitted flux and its relation to the underlying density contrast. In Section 3, we give details of the simulations that were used in our study. In Section 4, we present details of the modelling of the 3D flux. In Section 5.1, we derive the lower-order statistics for the flux in terms of that of the underlying density contrast. In Section 5.2, we provide a very brief introduction to the hierarchical ansatz, which we use to model the statistics of underlying density contrast. In Section 5.3, we provide the derivation of the PDF and the bias associated with the flux distribution. Finally, in Section 6, we discuss our results. We also provide a brief appendix, introducing the lognormal approximation as well as the hierarchical ansatz.

2 NOTATION

We use the following form of the Robertson–Walker line element for the background geometry of the Universe:

$$\mathrm{d}s^2 = -c^2\,\mathrm{d}t^2 + a^2(t)\left[\mathrm{d}r^2 + d_{\rm A}^2(r)(\mathrm{d}\theta^2 + \sin^2\theta\mathrm{d}\phi^2)\right]. \tag{1}$$

The angular position on the surface of the sky is specified by the unit vector $\hat{\Omega} = (\theta, \phi)$. The scalefactor of the Universe is given by $a(t)$. We have denoted the comoving angular diameter distance by $d_{\rm A}(r)$, where r denotes the comoving radial distance to redshift z: $d_{\rm A}(r) = K^{-1/2}\sin(K^{1/2}r)$ for positive curvature, $d_{\rm A}(r) = (-K)^{-1/2}\sinh[(-K)^{1/2}r]$ for negative curvature and r for the flat universe. For the present value of H_0 and $\Omega_{\rm M}$, we have $K = (\Omega_{\rm M} + \Omega_\Lambda - 1)\mathrm{H}_0^2$. The Hubble constant is denoted by H_0. The comoving radial distance $r(z)$ at a redshift z can be expressed through the following line-of-sight integration, with z' playing the role of intermediate redshift along the line of sight:

$$r(z) = \int_0^z \frac{\mathrm{d}z'}{\mathrm{H}_0\sqrt{\Omega_{\rm M}(1+z')^3 + \Omega_K(1+z')^2 + \Omega_\Lambda}}. \tag{2}$$

Throughout the paper, in our calculations, we adopt $\mathrm{H}_0 = 100\,h$ km s^{-1} Mpc^{-1} with $h = 0.7$ and $\sigma_8 = 0.87$. Here, $\Omega_{\rm M}$, Ω_Λ and Ω_K are the contributions of dark matter, vacuum energy and curvature to the cosmic density $\Omega_{\rm M} + \Omega_\Lambda + \Omega_K = 1$. For a flat universe, $\Omega_K = 0$.

3 SIMULATIONS

We use simulations that are run with the parallel hydrodynamical (TREESPH) code GADGET-2 based on the conservative 'entropy-formulation' of SPH (smooth particle hydrodynamics; Springel 2005). These consist of a cosmological volume with periodic boundary conditions filled with an equal number of dark matter and gas particles. Radiative cooling and heating processes were followed for a primordial mix of hydrogen and helium. We have assumed a mean UV background similar to that proposed by Haardt & Madau (1996), produced by quasars and galaxies as given by helium heating rates multiplied by a factor of 3.3, in order to better fit observational constraints on the temperature evolution of the IGM. This background gives a hydrogen ionization rate $\Gamma_{-12} \sim 1$ at the redshifts $z = 2$–4 of interest here (Bolton et al. 2005). The star formation criterion is a very simple; it is one that converts all the gas particles into stars whose temperature falls below 10^5 K and whose density contrast is larger than 1000 (it has been shown that the star formation criterion has a negligible impact on flux statistics). More details can be found in Viel et al. (2004b).

The cosmological reference model corresponds to a 'fiducial' ΛCDM universe with parameters, at $z = 0$, $\Omega_{\rm m} = 0.3$, $\Omega_\Lambda = 0.7$, $\Omega_{\rm b} = 0.05$, $n_{\rm s} = 1$, $H_0 = 70$ km s^{-1} Mpc^{-1} and $\sigma_8 = 0.85$. The initial conditions are generated at $z = 49$, using as linear matter power that extracted using the CAMB software. We have used 2×512^3 dark matter and gas particles in a volume of linear size $60\,h^{-1}$ comoving Mpc. The gravitational softening was set to $4\,h^{-1}$ kpc in comoving units for all particles. The mass per particle is 1.1×10^8 and 1.8×10^7 $\mathrm{M}_\odot\,h^{-1}$ for dark matter and gas particles, respectively. This simulation should have sufficient resolution to properly reproduce most of flux statistics, at least at $z \leq 3$ and marginally at $z = 4$. The flux power should, in fact, be converged with this set-up and also (marginally) the flux PDF. However, because we are dealing with projected quantities, we believe that numerical convergence issues are less severe than for other small-scale flux observables.

We select 128^2 grid points in the x–y plane and we interpolate along lines of sights parallel to the z-axis using a cloud-in-cell (CIC) algorithm. The Lyman α flux is also computed in redshift space along the same lines of sight by using the exact definition of transmitted flux and not the fluctuating Gunn–Peterson approximation. Peculiar velocities, neutral hydrogen fraction and gas temperature are calculated along the lines of sight and a Voigt profile is used to obtain the mock quasar spectra. The density and transmitted flux are then projected along the simulated lines of sight in the z-direction.

We model the star formation assuming a spatially uniform UV background. We apply a simple criterion for the star formation. This has been tested for the flux statistics previously in the regime we are using (Viel et al. 2004b; Bolton et al. 2008). Earlier studies have explicitly shown (e.g. Theuns et al. 1998) that such an approximation simply changes the amount of neutral hydrogen present in the cosmological volume without affecting the gas dynamics at an appreciable level. In effect, simulations can be run with a given UV background and then scaled to another (of different amplitude and shape), obtaining consistent results with a full hydrodynamic simulation. In our case, we have

chosen an UV background that is in agreement with observations and results in a reasonable evolution for the IGM temperature and mean flux level.

We would also like to stress that our simulated spectra are scaled to reproduce a given mean flux level, which is an observed quantity that has a small statistical scatter. The optical depth τ is proportional to the inverse of $[\Gamma_{-12}]$ (Γ_{-12} represents the amplitude of the ionizing background). Thus, scaling the spectra to reproduce a given mean flux is equivalent to scaling the UV background amplitude (a quantity which is known to much less precision than the mean flux) by a given factor (for further discussion, see Peeples et al. 2010).

4 LYMAN α FLUX AND THE IGM IN THREE DIMENSIONS

The fluctuating Gunn–Peterson approximation (Gunn & Peterson 1965) allows us to relate the transmitted flux $F_\alpha(z, \hat{\Omega})$ along a line of sight at a direction $\hat{\Omega} \equiv (\theta, \phi)$ at a redshift z with the fluctuation in neutral hydrogen density contrast $\tilde{\delta}$:

$$F_\alpha(z, \hat{\Omega}) = \exp\left\{-A(z)\left[1 + \tilde{\delta}(z, \hat{\Omega})\right]^\beta\right\}; \tag{3}$$

$$A(z) \equiv 0.0023(1+z)^{3.65}; \qquad \beta \equiv 2 - 0.7(\gamma - 1); \quad \gamma = 1.3. \tag{4}$$

The parameters $A(z)$ and β are two redshift-dependent functions relating the flux fluctuations to the dark matter overdensities. The parameter A is related to the level of mean transmitted flux, which is accurately measured (e.g. Kim et al. 2007). It also depends on inputs from baryonic physics, such as the baryonic fraction, IGM temperature and photoionization rate, as well as background cosmological parameters. The power-law index γ of the IGM temperature–density relation determines the value of the parameter β and is relatively independent of redshift z (Hui & Gnedin 1997; Kim et al. 2007) (of course, this is assuming that fluctuations in temperature because of, for example, reionization play a subdominant role). The allowed range of values for γ is $\gamma = (0.7\text{–}1.5)$. We use $\gamma = 1.3$ for our calculation, which is a good approximation to the actual value of the hydrodynamical simulation. Similarly, the uncertainty in measurement of $A(z)$ has been estimated from simulation and is given by $A(z) = 0.0023 \pm 0.0007(1+z)^{3.65\ \pm 0.21}$ (Kim et al. 2007).

Note that we expect a scatter around equation (4), which we have ignored (e.g. Viel et al. 2002). It is possible to incorporate such a scatter by convolving the theoretical PDF that we present with a noise PDF induced by such scatter.

4.1 PDF and bias in three dimensions

We use the lognormal distribution to model the distribution of $\tilde{\delta}$. The resulting flux PDF is obtained via a change of variable:

$$p(F_\alpha) = p(\tilde{\delta})\left|\frac{\mathrm{d}\tilde{\delta}}{\mathrm{d}F_\alpha}\right|; \qquad p\left[F_\alpha^{(1)}, F_\alpha^{(2)}\right] = p(\tilde{\delta}_1, \tilde{\delta}_2)\left|\frac{\mathrm{d}\tilde{\delta}_1}{\mathrm{d}F_\alpha^{(1)}}\right|\left|\frac{\mathrm{d}\tilde{\delta}_2}{\mathrm{d}F_\alpha^{(2)}}\right|. \tag{5}$$

In our notation, $\tilde{\delta}_{(i)} = \tilde{\delta}(\hat{\Omega}_i, z_i)$ and a similar notation is adopted for the fluxes along different lines of sight $F_\alpha^{(i)} = F_\alpha(\hat{\Omega}_i, z_i)$. For 3D studies, we have compared flux from neighbouring lines of sight at the same redshift. We have compared the PDFs using this approach for three different redshifts, $z = 2$, 3 and 4. The PDFs for $p(\delta)$ are constructed using lognormal prescriptions (equations B1 and B4).

The lognormal distribution is also used in the analysis based on the fitted column density distribution of absorption lines. In such studies, the lognormal distribution is introduced to relate $\tilde{\delta}$ and the number density of neutral hydrogen $n_{\mathrm{H\,I}}$. However, in relating the flux distribution and $\tilde{\delta}$, we assume that $\tilde{\delta}$ traces the underlying dark matter distribution, which can be described well by lognormal distribution. The lognormal distribution here is used to model the effect of gravity-induced non-linearity on PDFs of matter. A similar but somewhat different approach was used by Viel et al. (2002), who used lognormal approximation to map the density field to flux. In our case, we directly map the PDF of $\tilde{\delta}$ to that of the flux using simply a change of variable (equation 4). The construction of the PDF of $\tilde{\delta}$ is done using lognormal approximation as well as using extensions of perturbative methods (Valageas & Munshi 2004). These methods give nearly identical results. The hierarchical ansatz (introduced later; see Appendix B) is also used for the construction of one-point and two-point PDFs. It is interesting to point out that it has also been used by Valageas et al. (1999) to predict the clustering Lyman α absorbers. It was used to construct a unifying model from the clustering of low column-density clouds to the collapsed dense damped systems. The method that we present here is complementary to these studies because we directly probe the statistics of the transmitted flux. The theoretical predictions from lognormal model for PDF and bias are displayed in Fig. 1.

4.2 Numerical results in three dimensions

In Fig. 2, we have plotted the PDF of $p(\tilde{\delta})$ as a function of $\tilde{\delta}$. The PDF was computed by binning the data on a 128^3 grid. This allows us to resolve the PDF down to $O(10^{-6})$. The three panels show the PDF for three different redshifts. We also show the results from different analytical calculations. The two-point PDF (or 2PDF) denotes the joint PDF of $\tilde{\delta}$ at two different points. Typically, the 2PDF can be written as a product of two one-point PDFs at these two-point and additional correction terms. The corrective terms represents the contribution as a result of correlation. In general, in the large separation limit, when the two-point correlation is weak compared to the variance – that is, $\xi_{12}^\delta < \bar{\xi}_2^\delta$, where $\xi_{12}^\delta = \langle\delta(\boldsymbol{x}_1)\delta(\boldsymbol{x}_2)\rangle$ is the two-point correlation function and $\bar{\xi}_2$ is its volume average (the smoothing here refers to smoothing with a top-hat window characterized by a radius corresponding to the scales of the objects) – the 2PDF takes the following form in three

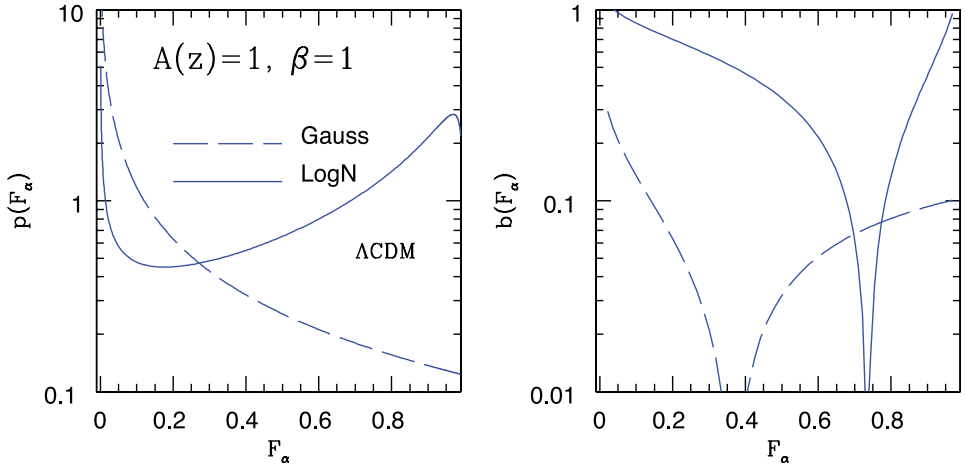

Figure 1. The PDF $p(F_\alpha)$ and bias $b(F_\alpha)$ of the flux F_α is plotted as a function of the flux F_α. The PDF (left panel) and the bias (right panel) are both constructed using a lognormal model for the underlying mass distribution. The resulting PDFs for $\tilde{\delta}$ are transformed into the flux PDFs using the fluctuating Gunn–Peterson approximation (equation 4). We compare the results from the lognormal approximation (solid lines) against those based on the Gaussian approximation (dashed lines). The values of $A(z)$ and β are constructed using the functional fit in equation (9) given by Kim et al. (2007); see text for more details. The bias changes signs at an intermediate flux value, which depends on the cosmological and hydrodynamical parameters that define the equation of state of the photoionized medium $A(z)$ and β. A fiducial value for the variance $\sigma = 3$ was assumed for this plot.

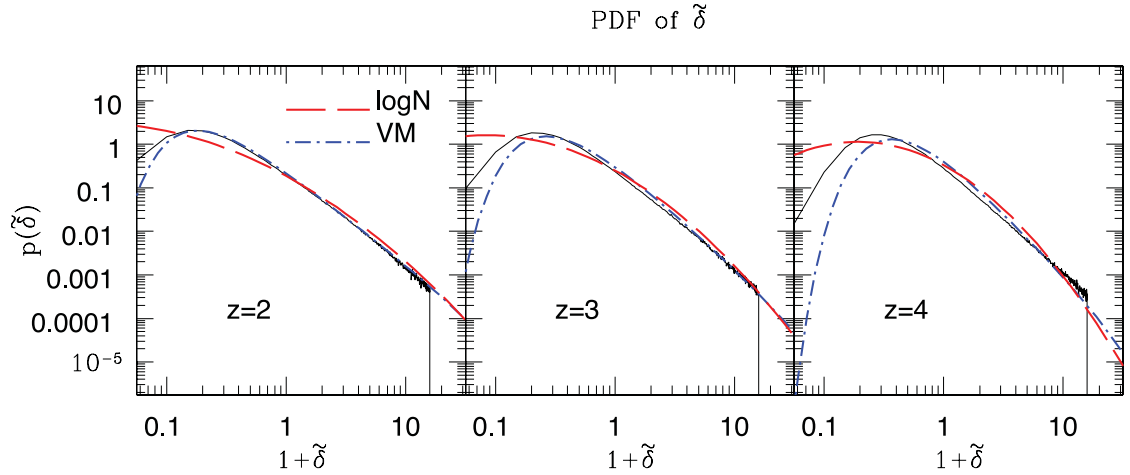

Figure 2. The PDF of the density contrast $p(\tilde{\delta})$ is displayed as a function of the density contrast $\tilde{\delta}$. The left ($z = 2$), middle ($z = 3$) and right ($z = 4$) panels correspond to the different redshifts z studied. Two different analytical models are displayed: the lognormal approximation (long-dashed lines) and the model proposed by Valageas & Munshi (2004) (dot-dashed lines), denoted as VM. The solid lines correspond to the results from simulations. Note that the analytical results and simulations for positive (overdense) δ values of the PDF agree extremely well for all three redshifts investigated in this work. The PDF was estimated using a 128^3 grid and this can resolve PDFs as low as $\mathcal{O}(10^{-6})$. However, the PDF becomes increasingly dominated by the presence or absence of rare large overdensities. The PDF is computed at the grid scale of a $60\,h^{-1}$ Mpc simulation box. We were trying to reach the smallest possible length-scale in our simulation, which is not affected by the resolution limit. Our aim was to test the lognormal model and the predictions by Valageas & Munshi (2004) as close to the Jeans length-scale as possible.

dimensions:

$$p(\tilde{\delta}_1, \tilde{\delta}_2)\mathrm{d}\tilde{\delta}_1\mathrm{d}\tilde{\delta}_2 = p(\tilde{\delta}_1)p(\tilde{\delta}_2)[1 + b(\tilde{\delta}_1)\xi_{12}^{\delta}b(\tilde{\delta}_2)]\mathrm{d}\tilde{\delta}_1\mathrm{d}\tilde{\delta}_2. \tag{6}$$

This equation describes the 2PDF $p(\delta_1, \delta_2)$ of the underlying density contrast δ in terms of PDFs $p(\delta)$ and bias $b(\delta)$. An identical relation also holds for $\tilde{\delta}$ above the Jeans scale. In general, the (differential) bias $b(\eta)$ is difficult to estimate. To increase the signal-to-noise, it is useful to compute the integrated bias beyond a threshold (Bernardeau 1994):

$$b(>\delta_0) \equiv \left[\frac{\int_{\delta_0}^{\infty} p(\tilde{\delta})b(\tilde{\delta})\mathrm{d}\tilde{\delta}}{\int_{\delta_0}^{\infty} p(\tilde{\delta})\mathrm{d}\tilde{\delta}}\right] = \frac{1}{\sqrt{\xi_{12}^{\delta}}}\left\{\frac{\int_{\delta_0}^{\infty}\int_{\delta_0}^{\infty} p(\tilde{\delta}_1, \tilde{\delta}_2)\mathrm{d}\tilde{\delta}_1\mathrm{d}\tilde{\delta}_2}{\left[\int_{\delta_0}^{\infty} p(\tilde{\delta})\mathrm{d}\tilde{\delta}\right]^2} - 1\right\}^{1/2}. \tag{7}$$

For our numerical estimation of bias associated with $\tilde{\delta}$, we have used equation (7) to compute the cumulative bias associated with $\tilde{\delta}$. Fig. 3 presents the numerical results for $b(>\delta_0)$ against the theoretical expectations from lognormal distribution. As expected, the lognormal distribution is quite accurate in predicting the numerical results for overdense regions. We show the results for three different redshifts relevant

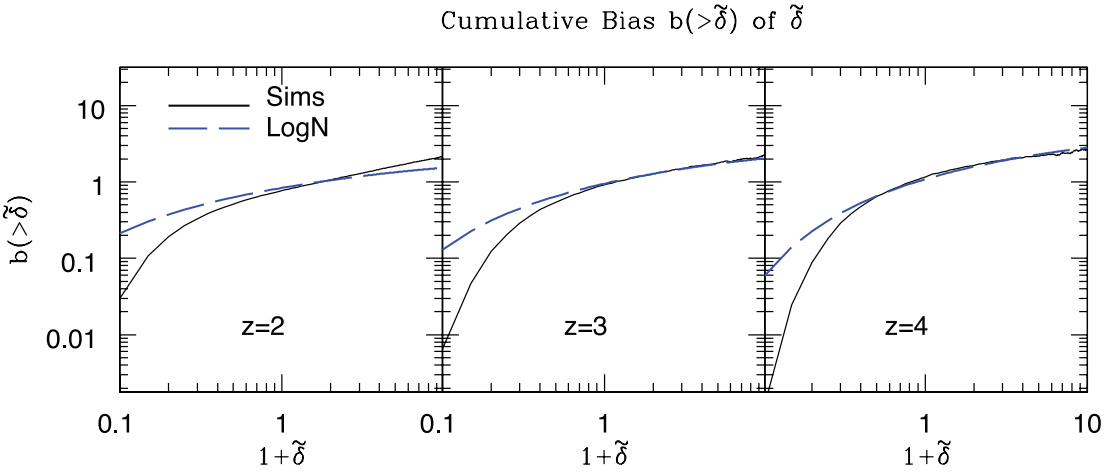

Figure 3. The cumulative bias of the density contrast $b(>\tilde{\delta})$ is displayed as a function of the density contrast $\tilde{\delta}$. The left ($z = 2$), middle ($z = 3$) and right ($z = 4$) panels correspond to different redshifts z. The lognormal approximation (long-dashed lines) and the results from simulations (solid lines) are displayed. The bias is constructed on a grid of 128^3. The lowest probability that can be estimated on this is grid is $\mathcal{O}(10^{-6})$. However, as mentioned previously, the higher $\tilde{\delta}$ tails of PDFs are increasingly dominated by the presence (or absence) of rare overdense (underdense) objects. The cumulative bias $b(>\tilde{\delta})$, which is a two-point statistics, is more affected by the finite size of the catalogue.

to high-redshift Lyman α studies. Note that the high $\tilde{\delta}$ tail of the PDF is reproduced well by the lognormal approximation (equation B5). The departure at lower $\tilde{\delta}$ is partly related to the smoothing introduced in hydrodynamical simulation during interpolation. Indeed, we only use the leading order term $\xi_{12}^{\delta}/\bar{\xi}^{\delta}$ in our calculation of bias from the lognormal distribution. These results are valid in the large separation limit. Additional corrective terms can be included if necessary. In Fig. 4 we have displayed simulated Lyman α flux and projected gas density for redshifts $z = 1$, 3 and 4.

Using the transformation given in equation (5), we can express the PDF $p(F_\alpha)$ and bias $b(<F_\alpha)$ in terms of the PDF $p(\delta_0)$ and bias for the density $b(>\delta_0)$:

$$b(>\delta_0) \equiv \frac{1}{\sqrt{\xi_{12}^{\delta}}}\left\{\frac{\int_{\delta_0}^{\infty}\int_{\delta_0}^{\infty} p(\tilde{\delta}_1,\tilde{\delta}_2)\mathrm{d}\tilde{\delta}_1\mathrm{d}\tilde{\delta}_2}{[\int_{\delta_0}^{\infty} p(\tilde{\delta})\mathrm{d}\tilde{\delta}]^2} - 1\right\}^{1/2} = \frac{1}{\sqrt{\xi_{12}^{\delta}}}\left\{\frac{\int_0^{F_\alpha}\int_0^{F_\alpha} p[F_\alpha^{(1)},F_\alpha^{(2)}]\mathrm{d}F_\alpha^{(1)}\mathrm{d}F_\alpha^{(2)}}{[\int_0^{F_\alpha} p(F_\alpha)\mathrm{d}F_\alpha]^2} - 1\right\}^{1/2} \equiv \sqrt{\frac{\xi_\alpha}{\xi_\delta}} \quad b(<F_\alpha). \tag{8}$$

The results of such a calculation for the PDF are shown in Fig. 5. There is no accurate model for bias in the highly non-linear regime. The lognormal approximation is accurate in the quasi-linear regime and starts to fail in the highly non-linear regime. The approach taken by Valageas & Munshi (2004) can be extended to the construction of bias. The results of integrated bias for the flux are defined in equation (8) and plotted in Fig. 6. We have found that including a power-law mapping $(1+\delta) \rightarrow (1+\delta)^{\Delta}$, where Δ is a constant of order unity, can fit the numerical results, if it is applied before the exponential transformation.

5 PROJECTED FLUX DECREMENT

We are interested in scales larger than the comoving Jeans length, at around redshift $z = 3$, which is about $1\,h^{-1}$ Mpc. The fractional flux $\delta\mathcal{F}_\alpha(z,\hat{\Omega})$ in this limit can be related to the underlying dark matter density distribution δ, using equation (3), with the following expression:

$$\delta F_\alpha(z,\hat{\Omega}) \equiv \left[F_\alpha(z,\hat{\Omega}) - \langle F_\alpha(z,\hat{\Omega})\rangle\right]/\langle F_\alpha(z,\hat{\Omega})\rangle = -A(z)\beta(z)\tilde{\delta}(\hat{\Omega},z) \approx -A(z)\beta(z)b(z)\delta(\hat{\Omega},z). \tag{9}$$

The relation assumes that the IGM traces the dark matter distribution at larger scales (above the Jeans length). We have incorporated an additional redshift-dependent bias factor $b(z)$ in relating $\delta_{\rm IGM}(z)$ and $\delta(z)$, for generality. The results presented here can be generalized for arbitrary redshift-dependent bias. In our calculations, we set $b(z) = 1$. The factors $A(z)$ and β have already been introduced; see, for example, Hui & Gnedin (1997) and McDonald (2003) for a discussion of the temperature–density relation, which is well described by a power law.

The integrated flux decrement $\delta\mathcal{F}_\alpha(\hat{\Omega})$ towards a particular direction $\hat{\Omega}$ can be expressed through a line-of-sight integration as a projected density contrast:

$$\delta\mathcal{F}_\alpha(\hat{\Omega}) = \int_{r_i}^{r_q} \mathrm{d}r\ \delta F_\alpha(\hat{\Omega},r) \approx \int_{r_i}^{r_q} \mathrm{d}r\, A(r)\beta(r)\tilde{\delta}(\hat{\Omega},r) \equiv \int_{r_i}^{r_q} \mathrm{d}r\ \omega_\alpha(r)\ \tilde{\delta}(\hat{\Omega},r). \tag{10}$$

The range of comoving distances probed by the Lyman α spectrum extends from r_i to the quasar distance r_q. We define a parameter $\delta\mathcal{F}_\alpha^{\rm min} = -\int_{r_i}^{r_q} w_\alpha(r)\,\mathrm{d}r$, which is the minimum value of $\delta\mathcal{F}_\alpha$ for given r_i and r_q. The weight $w_\alpha(z)$, which acts as a kernel for projection, can be expressed in terms of previously introduced functions $w(z) = A(z)\beta(z)$. A few comments are in order. The assumption of quasi-linear theory (e.g. the lognormal model) is expected to be valid above the Jeans length. This is where our results are expected to be valid (Eisenstein & Hu 1998). The relationship between the flux and the underlying mass distribution has been verified in numerous studies (Bi & Davidson 1997; Croft et al. 2002; Viel et al. 2002; Saitta et al. 2008; McQuinn et al. 2009). It is also important to note that the simple linear relationship, which is often used to derive many analytical results in the context of Lyman α studies, can be modified in the presence of any non-gravitational

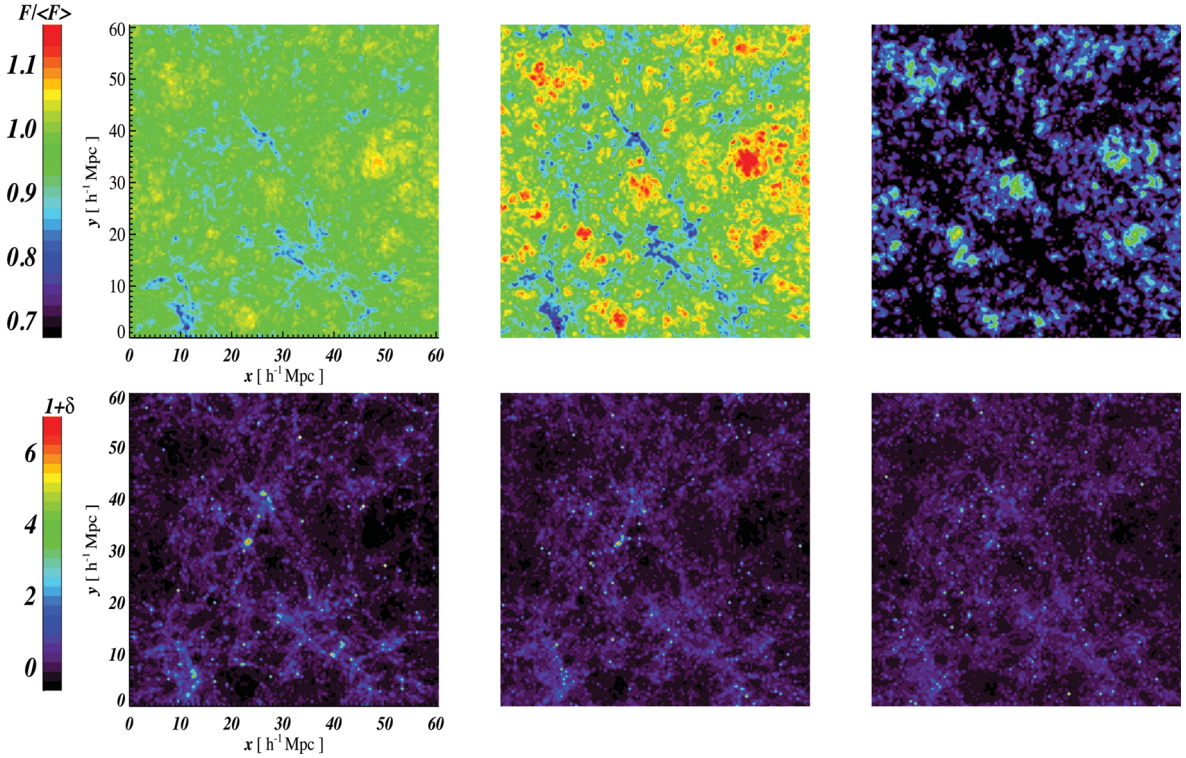

Figure 4. We show the projected transmitted Lyman α flux (top panels) and projected gas density (bottom panels) in the simulated volume at $z = 2$, 3 and 4 (left, middle and right columns, respectively). The gas density is extracted at 128^3 grid points using a CIC interpolation scheme; the values shown in the bottom panels are the projected $\tilde{\delta}$ along 128^2 lines of sight (along the z-axis). The growth of the cosmic structures can be appreciated from high to low redshift. In the upper panels, we show the mean value $\langle F_\alpha \rangle$ along the same 128^2 lines of sight. The values at the three redshifts are all normalized to the $\langle F_\alpha(z=2) \rangle$ value and the spectra are simulated by using the exact definition of the transmitted flux and not approximations. Because the mean flux is a strongly evolving function of redshift, the growth of cosmic structure in the Lyman α flux is more difficult to interpret than in the corresponding density slices, and simulations and/or models are needed. In the upper panels, voids correspond to regions of high transmissivity, while dense regions produce absorptions. At $z = 2$, the $\langle F_\alpha \rangle$ values fluctuate by about 10 per cent around the mean, while at $z = 4$, this value becomes 20 per cent (because the mean transmitted flux is about two times smaller at this redshift). The simulation refers to a hydrodynamical run with 2×512^3 gas and dark matter particles in a 60^3 (Mpc h^{-1})^3 periodic comoving volume.

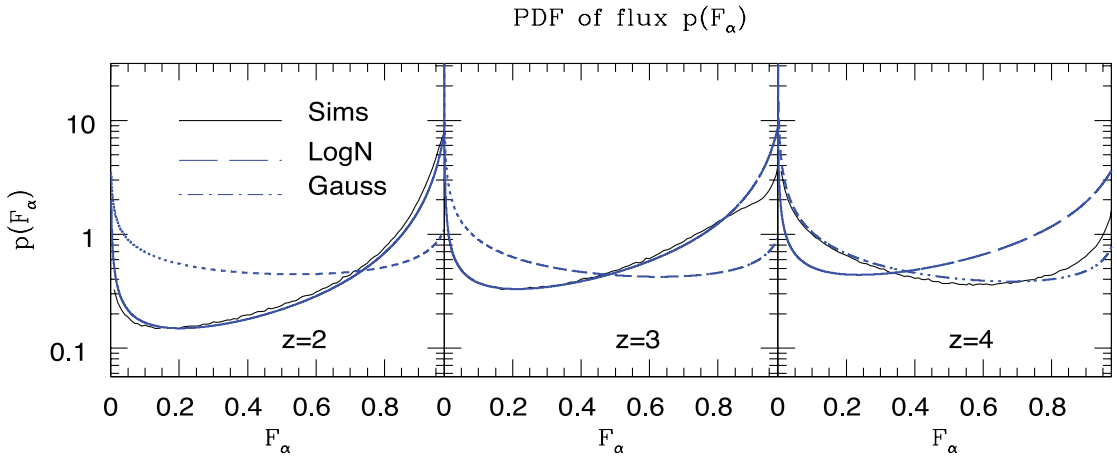

Figure 5. The PDF of the flux $p(F_\alpha)$ as a function of the flux F_α. The left ($z = 2$), middle ($z = 3$) and right ($z = 4$) panels correspond to different redshifts z. Two different analytical models are displayed: the lognormal approximation (long-dashed lines) and the Gaussian approximation (dot-dashed lines). The flux PDF is constructed from the PDF of $\tilde{\delta}$ using equation (4). The results from the simulation are also depicted (solid lines).

process, such as fluctuations in the level of UV radiation or temperature fluctuation. Such non-gravitational effects are harder to model analytically. Next, we use these expressions to model the lower-order statistics of $\delta\mathcal{F}_\alpha(\hat{\Omega})$.

We would like to add a cautionary note here. Our use of the linear-order relation (i.e. equation 9) can be improved by adding higher-order corrections to construct a more accurate PDF. The approach here should be seen as a mean linear fit, which is valid over a finite range of $\hat{\delta}$. This is justified, given the uncertainty associated with the parameters $A(z)$ and $\beta(z)$.

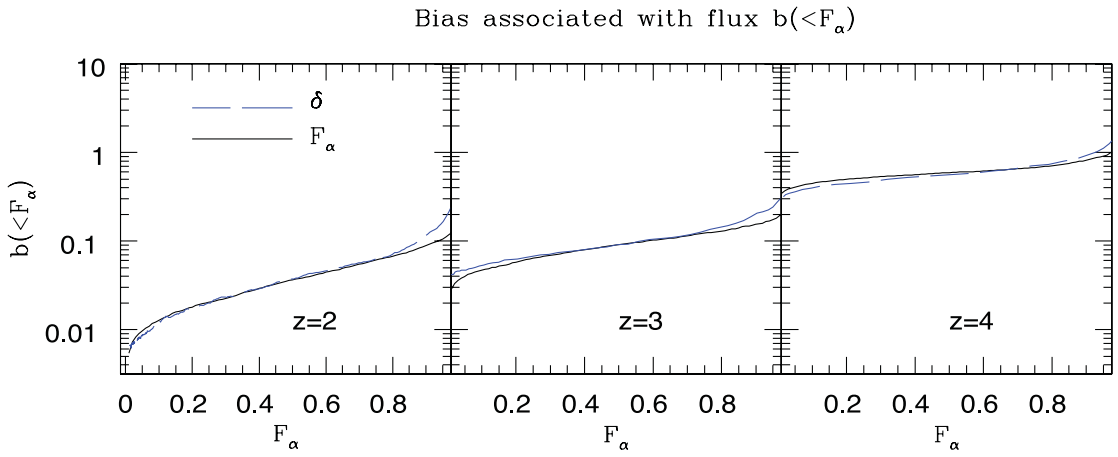

Figure 6. The bias of the flux $b(<F_\alpha)$ as a function of the flux F_α. The left ($z = 2$), middle ($z = 3$) and right ($z = 4$) panels correspond to different redshifts z. The solid lines correspond to direct estimates from 3D flux maps. The dashed lines are from maps that are generated from the density maps.

5.1 Lower-order cumulants and cumulant correlators in projection

We use both cumulants and cumulant correlators in our studies. The one-point cumulants can be estimated from a single line of sight whereas neighbouring pairs of QSOs are required to probe the cumulant correlators. By construction, the normalized cumulant correlators are independent of the separation of quasar pairs. Increasing the number of lines of sight will help to increase the signal-to-noise.

To compute the variance and other lower-order moments or cumulants, we start with the Fourier transform of the 3D density contrast δ, which we denote as $\delta(\boldsymbol{k})$:

$$\delta\mathcal{F}_\alpha(\hat{\Omega}) = \int_{r_i}^{r_q} \mathrm{d}r\ \omega_\alpha(r) \int \frac{\mathrm{d}^3\boldsymbol{k}}{(2\pi)^3} \exp\left[\mathrm{i}rk_\parallel + \mathrm{i}d_\mathrm{A}(r)\boldsymbol{\theta}_{12}\cdot\boldsymbol{k}_\perp\right] \delta(\boldsymbol{k}, r). \tag{11}$$

Here, $\boldsymbol{\theta}_{12}$ denotes the angle between the line-of-sight direction $\hat{\Omega}$, which should be treated as a vector on the surface of the sky, and the wave vector $\boldsymbol{k}$, and $k_\parallel$ and $\boldsymbol{k}_\perp$ denote the components of $\boldsymbol{k}$, parallel and perpendicular to the line of sight direction. In the small-angle approximation, we assume that $|\boldsymbol{k}_\perp| \gg k_\parallel$. Using these definitions, we can compute the projected variance $\langle\delta\mathcal{F}_\alpha^2\rangle$ in terms of the dark matter power spectrum $P_\delta(k, r)$ (Kaiser 1992):

$$\left\langle\delta\mathcal{F}_\alpha^2(\hat{\Omega})\right\rangle_c = \int_{r_i}^{r_q} \mathrm{d}r \frac{\omega_\alpha^2(r)}{d_\mathrm{A}^2(r)} \int \frac{\mathrm{d}^2\boldsymbol{l}}{(2\pi)^2}\, \mathrm{P}_\delta\left[\frac{l}{d_\mathrm{A}(r)}, r\right]. \tag{12}$$

Similarly, the higher-order moments of the field relate $\langle\delta\mathcal{F}_\alpha^p\rangle$ to the 3D multispectra of the underlying dark matter distribution B_p (Hui 1999; Munshi & Coles 2000):

$$\left\langle\delta\mathcal{F}_\alpha^p(\hat{\Omega})\right\rangle_c = \int_{r_i}^{r_q} \mathrm{d}r \frac{\omega_\alpha^p(r)}{d_\mathrm{A}^{2(p-1)}(r)} \int \frac{\mathrm{d}^2\boldsymbol{l}_1}{(2\pi)^2} \cdots \int \frac{\mathrm{d}^2\boldsymbol{l}_p}{(2\pi)^2} \mathrm{B}_\delta^{(p)}\left(\frac{l_1}{d_\mathrm{A}(r)}, \cdots, \frac{l_p}{d_\mathrm{A}(r)}\right)_{\sum l_i = 0}. \tag{13}$$

The subscript c denotes the connected part of a diagram that represents the higher-order correlation function; the Limbers approximation (Limber 1954) is used to derived the above result. The subscript $\sum \boldsymbol{l}_i = 0$ denotes a multiplicative Dirac delta function $\delta_\mathrm{D}[\sum_{i=1}^p(\boldsymbol{l}_i)]$. We have used the compact notation $B_\delta^{(p)}$ to denote the pth-order multispectra where $B_\delta^{(3)}$ denotes the bispectrum and $B_\delta^{(4)}$ denotes the trispectrum, often denoted as T_δ in the literature. The power spectrum correspond to $B_\delta^{(2)}$. We use these results to show that it is possible to compute the complete PDF of $\delta\mathcal{F}_\alpha$ from the underlying dark matter PDF. The details of the analytical results presented here can be found in Munshi & Jain (2000, 2001).

In addition to the cumulants, their correlators are important because they are related to the 2PDF, and hence the bias associated with the higher flux regions

$$\left\langle\delta\mathcal{F}_\alpha^p(\hat{\Omega}_1)\delta\mathcal{F}_\alpha^q(\hat{\Omega}_1)\right\rangle_c = \int_{r_i}^{r_q} \mathrm{d}r \frac{\omega_\alpha^{p+q}(r)}{d_\mathrm{A}^{2(p+q-1)}(r)} \int \frac{\mathrm{d}^2\boldsymbol{l}_1}{(2\pi)^2} \cdots \int \frac{\mathrm{d}^2\boldsymbol{l}_{p+q}}{(2\pi)^2} \mathrm{B}_\delta^{(p+q)}\left[\frac{l_1}{d_\mathrm{A}(r)}, \cdots, \frac{l_{p+q}}{d_\mathrm{A}(r)}\right]_{\sum_i l_i = 0}. \tag{14}$$

A special case of this equation corresponds to the expression for the two-point correlation function $\langle\delta\mathcal{F}_\alpha^p(\hat{\Omega}_1)\delta\mathcal{F}_\alpha^q(\hat{\Omega}_1)\rangle$. Here, T are generic, and we specialize them by assuming a particular form for the higher-order multispectra to make further progress. Just as for the normalized cumulants S_p, we can define the normalized cumulant correlators $C_{pq} = \langle\delta\mathcal{F}_\alpha^p(\hat{\Omega}_1)\delta\mathcal{F}_\alpha^q(\hat{\Omega}_1)\rangle / \langle\delta\mathcal{F}_\alpha(\hat{\Omega}_1)\delta\mathcal{F}_\alpha(\hat{\Omega}_1)\rangle\langle\delta\mathcal{F}_\alpha^2(\hat{\Omega})\rangle$. We use the normalized cumulants or the S_p parameters and the normalized cumulant correlators to construct the PDF and the bias associated with the flux decrements or $\delta\mathcal{F}_\alpha$. We denote the normalized cumulants and their correlators of density by S_p and C_{pq}, respectively. The corresponding quantities for the flux decrements are denoted using a superscript α (i.e. S_p^α and C_{pq}^α).

5.2 A minimal tree model

The spatial length-scales, corresponding to the small angular scales, which are relevant in our discussion, are in the highly non-linear regime. Assuming a minimal tree model (see Munshi et al. 2008, for more details) for the matter correlation hierarchy in the highly non-linear regime, we can write the general form of the Nth-order correlation function $\xi_\delta^{(p)}$ as a product of the two-point correlation function $\xi_\delta^{(2)}$ (Davis & Peebles 1977; Groth & Peebles 1977; Fry 1984; Balian & Schaeffer 1989; Szapudi & Szalay 1993, 1997). In Fourier space, such an ansatz means that the hierarchy of multispectra can be written as sums of products of the matter power spectrum:

$$B_\delta(\boldsymbol{k}_1,\boldsymbol{k}_2,\boldsymbol{k}_3)_{\sum k_i=0} = Q_3\left[P_\delta(k_1)P_\delta(k_2)+P_\delta(k_2)P_\delta(k_3)+P_\delta(k_3)P_\delta(k_1)\right]; \tag{15}$$

$$T_\delta(\boldsymbol{k}_1,\boldsymbol{k}_2,\boldsymbol{k}_3,\boldsymbol{k}_4)_{\sum k_i=0} = R_a\ P_\delta(k_1)P_\delta(|\boldsymbol{k}_1+\boldsymbol{k}_2|)P_\delta(|\boldsymbol{k}_1+\boldsymbol{k}_2+\boldsymbol{k}_3|)+\text{cyc.perm.}+R_b\ P_\delta(k_1)P_\delta(k_2)P_\delta(k_3)+\text{cyc.perm.} \tag{16}$$

The subscript $\sum k_i=0$ represents a Dirac δ function $\delta_{\rm D}[\sum_{i=1}^{p}(\boldsymbol{k}_i)]$. Different hierarchical models differ in the way they specify the amplitudes Q_3, R_a, R_b, etc. The results that we derive for higher-order correlation functions are valid for the stellar model (a detailed discussion can be found, for example, in Barber, Munshi & Valageas 2004):

$$\left\langle\delta\mathcal{F}_\alpha^3\right\rangle_c = (3Q_3)\mathcal{C}_3\left\{\left[\mathcal{J}_0^\alpha(r)\right]^2\right\} = S_3^\alpha\left\langle\delta\mathcal{F}_\alpha^2\right\rangle_c^2; \qquad \left\langle\delta\mathcal{F}_\alpha^4\right\rangle_c = (12R_a+4R_b)\mathcal{C}_4\left\{\left[\mathcal{J}_0^\alpha(r)\right]^3\right\} = S_4^\alpha\left\langle\delta\mathcal{F}_\alpha^2\right\rangle_c^3, \tag{17}$$

Here, we have defined the following quantities:

$$\mathcal{C}_p\left\{\left[\mathcal{J}_0^\alpha(r)\right]^{p-1}\right\} = \int_{r_i}^{r_q}\frac{\omega_\alpha^p(r)}{d_{\rm A}^{2(p-1)}(r)}\left[\mathcal{J}_0^\alpha(r)\right]^{(p-1)}{\rm d}r; \qquad \left[\mathcal{J}_0^\alpha(r)\right] = \int\frac{d^2\boldsymbol{l}}{(2\pi)^2}P_\delta\left[\frac{l}{d_{\rm A}(r)}\right]. \tag{18}$$

These lower-order moments are then used to construct the void probability function (VPF), which also acts as a generating function for the normalized S_p^α parameters for flux decrement $\delta\mathcal{F}_\alpha(\hat{\Omega})$. The PDF can be constructed from the knowledge of the VPF, as detailed in the next section.

5.3 Probability distribution function of transmitted flux

Before we discuss our techniques to construct the PDF for the projected transmitted flux, a few explanations regarding the notation and its link to the entire hierarchical paradigm are necessary. Although our primary aim is to construct the PDF, it is usually easier to construct the moment generating function $\phi(y)$, which is introduced later. The lower-order normalized cumulants (also known as the S_p parameters), up to an arbitrary order, can be recovered, if necessary, using a Taylor expansion of $\phi(y)$. The function $h(x)$ is related to $\phi(x)$ through an inverse Laplace transform [i.e. a knowledge of S_p parameters to an arbitrary order can be used to construct the function $h(x)$]. However, the function $h(x)$ is simply a scaled PDF and the real PDF can be extracted from it using the definition of scaling variable x (to be defined later).

The construction of PDF for $\delta\mathcal{F}_\alpha$ involves additional steps. First, the generating function $\Phi^\alpha(y)$ for the lower-order normalized cumulants S_p^α is expressed in terms of the underlying $\phi(y)$. Next, we define a new scaling variable for $\delta\mathcal{F}_\alpha$, which is denoted by η. We show that, under a certain simplifying approximation, the cumulant generating function for η [i.e. $\Phi^\eta(y)$] is the same as the underlying cumulant generating function $\phi(y)$. Once this is proved, it is easy see that the scaled PDFs $H^\eta(y)$ and $h(y)$ are also the same because they are simply the Laplace transforms of $\Phi^\eta(y)$ and $\phi(y)$, respectively. This technique that we have used has already been used to derive similar relations in the context of weak lensing statistics (Bernardeau & Valageas 2000; Munshi & Jain 2000, 2001; Valageas 2000).

The generating function $\Phi^\alpha(y)$ (or the VPF) for the lower-order normalized cumulants S_p^α for the flux decrement $\delta\mathcal{F}_\alpha(\hat{\Omega})$ can be expressed as

$$\Phi^\alpha(y) \equiv \sum_{p=1}\frac{S_p^\alpha}{p!}y^p = y+\sum_{p=2}^{\infty}\frac{\langle\delta\mathcal{F}_\alpha^p(\hat{\Omega})\rangle_c}{\langle\delta\mathcal{F}_\alpha^2(\hat{\Omega})\rangle_c^{p-1}}y^p. \tag{19}$$

Our aim is to relate the VPF $\Phi^\alpha(y)$ and $\phi(y)$, where $\phi^\alpha(y)$ is the VPF of the underlying matter distribution. The exact functional form of $\phi(y)$ is fixed by our choice of the stellar model. Using equation (17), we can write

$$\Phi^\alpha(y) = \int_{r_i}^{r_q}\sum_{p=1}^{\infty}\frac{1}{p!}S_p\frac{\omega_\alpha^p(r)}{d_{\rm A}(r)^{2(p-1)}}\left[\mathcal{J}_0^\alpha(r)\right]^{(p-1)}\frac{y^p}{\langle\delta\mathcal{F}_\alpha^2\rangle_c^{(p-1)}}-y\delta\mathcal{F}_\alpha^{\rm min}. \tag{20}$$

Using the VPF of the underlying mass distribution $\phi(x)$, the above expression can be rewritten in a more compact form:

$$\Phi^\alpha(y) = \int_{r_i}^{r_q}{\rm d}r\ d_{\rm A}^2(r)\left[\frac{\langle\delta\mathcal{F}_\alpha^2\rangle_c}{\mathcal{J}_0^\alpha(r)}\right]\phi\left[\frac{\omega_\alpha(r)}{d_{\rm A}^2(r)}\frac{\mathcal{J}_0^\alpha(r)}{\langle\delta\mathcal{F}_\alpha^2\rangle_c}y\right]; \qquad \phi(y) = \sum_p\frac{S_p}{p!}y^p. \tag{21}$$

We define a variable η that will make the analysis simpler. The VPF for η, denoted $\Phi^\eta(y)$, can now be expressed in terms of the VPF of the underlying mass distribution $\phi(y)$ using the following expression:

$$\Phi^\eta(y) = \frac{1}{|\delta\mathcal{F}_\alpha^{\rm min}|}\int_{r_i}^{r_q}{\rm d}r\ \left[\frac{d_{\rm A}^2(r)\langle\delta\mathcal{F}_\alpha^2\rangle_c}{\mathcal{J}_0^\alpha(r)|\delta\mathcal{F}_\alpha^{\rm min}|}\right]\phi\left[|\delta\mathcal{F}_\alpha^{\rm min}|\frac{\omega_\alpha(r)}{d_{\rm A}^2(r)}\frac{\mathcal{J}_0^\alpha(r)}{\langle\delta\mathcal{F}_\alpha^2\rangle_c}y\right]; \qquad \eta = \frac{\delta\mathcal{F}_\alpha-\delta\mathcal{F}_\alpha^{\rm min}}{\delta\mathcal{F}_\alpha^{\rm min}}. \tag{22}$$

The scaling properties of the PDF in an hierarchical model are encoded in a scaling function. The scaling function $H^\eta(x)$ is related to the PDF of η, that is, $p(\eta)$, whereas the scaling function $h(x)$ is associated with the PDF of the underlying mass distribution δ. The following relation

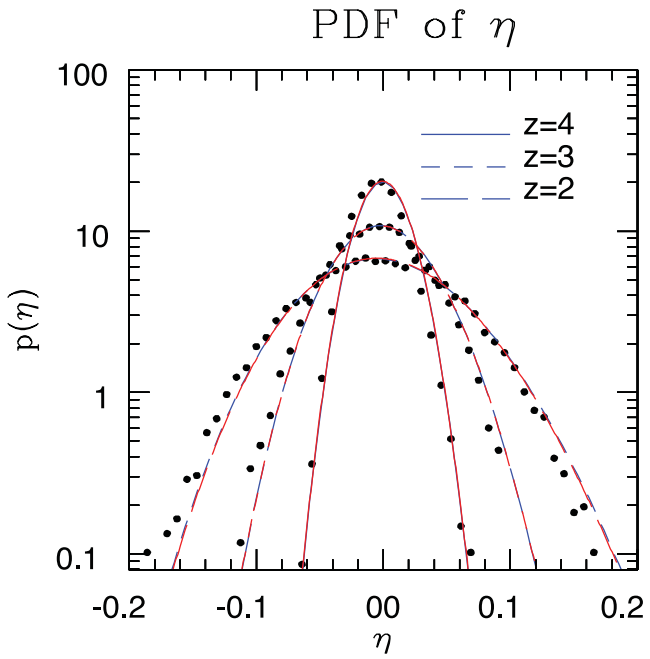

Figure 7. The PDF of the projected flux decrement $p(\delta\mathcal{F}_\alpha)$ is plotted. The two different approximations that we have studied produce nearly identical results. Three different redshifts are shown. The lower (higher) redshift corresponds to broader (narrower) distribution. The lines of sight are drawn from a 512^3 simulation box. A total of 512^2 lines of sight are analysed, which are distributed on a regular grid.

relates $H^\eta(x)$ and the scaling function $h(x)$:

$$H^\eta(x) = \frac{1}{|\delta\mathcal{F}_\alpha^{\rm min}|}\int_{r_i}^{r_q} w_\alpha(r){\rm d}r\ \left[\frac{d_{\rm A}^2(r)\langle\delta\mathcal{F}_\alpha^2\rangle_c}{\mathcal{J}_0^\alpha(r)|\delta\mathcal{F}_\alpha^{\rm min}|w_\alpha(r)}\right]^2 h\left[\frac{x\langle\delta\mathcal{F}_\alpha^2\rangle_c d_{\rm A}^2(r)}{w_\alpha(r)|\delta\mathcal{F}_\alpha^{\rm min}|\mathcal{J}_0^\alpha(r)}\right]. \tag{23}$$

The above relation is derived using the following definition of $H^\eta(x)$ in terms of the moment generating function or VPF $\Phi^\eta(y)$ (Balian & Schaeffer 1989) because the moment generating function $\Phi^\eta(y)$ and the scaled PDF $H^\eta(x)$ are linked through an inverse Laplace transform:

$$H^\eta(x) = -\int_{-{\rm i}\infty}^{{\rm i}\infty}\frac{{\rm d}y}{2\pi{\rm i}}\exp(xy)\Phi^\eta(y). \tag{24}$$

A similar result holds for $h(x)$ and $\phi(y)$. Using an approximate form for the integrals, we recover the following relation:

$$p_\alpha(\delta\mathcal{F}_\alpha) = p(\eta)/|\delta\mathcal{F}_\alpha^{\rm min}|. \tag{25}$$

In terms of the cumulants, this means $S_p^\alpha = S_p/|\delta\mathcal{F}_\alpha^{\rm min}|^{p-2}$. It is instructive to note that the final result is independent of any detailed modelling. We use a lognormal PDF as well as the PDF constructed using the hierarchical ansatz to model $p(\eta)$.

It is important to note that the function $h(x)$ is fundamental to all scaling analysis. It was initially introduced to study the clustering of galaxies and was later used in diverse cosmological studies (e.g. Valageas et al. 1999). For example, the mass functions of collapsed objects, including clusters, groups and galaxies, can all be described by the scaling function $h(x)$. The multiplicity function $\eta(M, z)$ at redshift x for collapsed objects of mass M can be expressed by $\eta(M, z){\rm d}M/M = (\bar{\rho}/M)xh(x)\,{\rm d}x$. Here, the scaling function x can be expressed as $x = [1 + \delta(M, z)]/\bar{\xi}_2$ and $\bar{\rho}$ is the mean physical density of the Universe. Thus, scaling arguments can also provide an alternative to the usual mass function calculation, based on the Press–Schecter formalism. These issues have been discussed extensively in the literature (e.g. Valageas & Schaeffer 2000a). The volume-averaged two-point correlation function $\bar{\xi}_2$ is evaluated at a corresponding relevant scale. It is interesting to note that the functional form for the scaling function $h(x)$ depends only on the form for the initial power spectrum and its qualitative behaviour can be predicted using very general arguments. Two different asymptotes are particularly well understood: (i) $x \ll 1$: $h(x) \propto x^{\omega-2}$ and (ii) $x \gg 1 : h(x) \propto x^{\omega_s-1}\exp(-x/x_\star)$ with $\omega \sim 0.5$ and $\omega_s \sim -3/2$. A more detailed discussion about some of the salient features can be found in Appendix A.

The numerical results for the 2D PDF of η are presented in Fig. 7. The results are depicted for three redshifts, $z = 2$, 3 and 4. These results were computed using a grid of 512^2 lines of sight drawn from a 512^3 simulation box.The underlying cosmology is same as those adopted for 3D studies. The resulting PDFs computed using this grid are stable down to $O(10^{-4})$. Note that the projected PDF is closer to a Gaussian in form than its 3D counterpart.

5.4 Joint PDF of flux decrements of neighbouring quasar spectra

The 2PDF is constructed from the cumulant correlators, which can be constructed by correlating the flux decrements of neighbouring lines of sight $\hat{\Omega}_1$ and $\hat{\Omega}_2$. The cumulant correlators are two-point statistics and generalize the usual two-point correlation function to higher orders

that have the ability to probe non-Gaussianity. More interestingly, they are related to the bias associated with high flux-decrement regions:

$$C^{\alpha}_{pq} = \langle \delta\mathcal{F}_\alpha(\hat{\Omega}_1)^p \delta\mathcal{F}_\alpha(\hat{\Omega}_2)^q \rangle_c / \left\langle \delta\mathcal{F}^2_\alpha(\hat{\Omega}) \right\rangle_c^{p+q-2} \langle \delta\mathcal{F}_\alpha(\hat{\Omega}_1)\delta\mathcal{F}_\alpha(\hat{\Omega}_2)\rangle_c. \tag{26}$$

Note that, by construction, $C_{11} = 1$, which is a result of the particular normalization that is generally adopted for C_{pq}. At the lower order, the cumulant correlators can be expressed in terms of the hierarchical amplitudes (i.e. Q_3, R_a, R_b, S_a, S_b, S_c):

$$\left\langle \delta\mathcal{F}^2_\alpha(\hat{\Omega}_1)\delta\mathcal{F}_\alpha(\hat{\Omega}_2) \right\rangle_c = 2Q_3\mathcal{C}_3\left[\mathcal{J}^\alpha_0 \mathcal{J}^\alpha_{12}\right] = C^\eta_{21}\mathcal{C}_3\left[\mathcal{J}^\alpha_0 \mathcal{J}^\alpha_{12}\right] \equiv C^\alpha_{21}\left\langle \delta\mathcal{F}^2_\alpha \right\rangle_c \left\langle \delta\mathcal{F}_\alpha(\hat{\Omega}_1)\delta\mathcal{F}_\alpha(\hat{\Omega}_2) \right\rangle_c; \tag{27}$$

$$\left\langle \delta\mathcal{F}^3_\alpha(\hat{\Omega}_1)\delta\mathcal{F}(\hat{\Omega}_2) \right\rangle_c = (3R_a + 6R_b)\mathcal{C}_4\left[(\mathcal{J}^\alpha_0)^2 \mathcal{J}^\alpha_{12}\right] = C^\eta_{31}\mathcal{C}_4\left[(\mathcal{J}^\alpha_0)^2 \mathcal{J}^\alpha_{12}\right] \equiv C^\alpha_{31}\left\langle \delta\mathcal{F}^2_\alpha \right\rangle_c^2 \left\langle \mathcal{F}(\hat{\Omega}_1)\mathcal{F}(\hat{\Omega}_2) \right\rangle_c; \tag{28}$$

$$\left\langle \mathcal{F}^2_\alpha(\hat{\Omega}_1)\mathcal{F}^2_\alpha(\hat{\Omega}_2) \right\rangle_c = 4R_b\mathcal{C}_4\left[(\mathcal{J}^\alpha_0)^2 \mathcal{J}^\alpha_{12}\right] = C^\eta_{22}\mathcal{C}_4\left[(\mathcal{J}^\alpha_0)^2 \mathcal{J}^\alpha_{12}\right] \equiv C^\alpha_{22}\left\langle \mathcal{F}^2 \right\rangle_c^2 \left\langle \delta\mathcal{F}_\alpha(\hat{\Omega}_1)\delta\mathcal{F}_\alpha(\hat{\Omega}_2) \right\rangle_c; \tag{29}$$

$$\left\langle \delta\mathcal{F}^4_\alpha(\hat{\Omega}_1)\delta\mathcal{F}_\alpha(\hat{\Omega}_2) \right\rangle_c = (24S_a + 36S_b + 4S_c)\mathcal{C}_5\left[(\mathcal{J}^\alpha_0)^3 \mathcal{J}^\alpha_{12}\right] = C^\eta_{41}\mathcal{C}_5\left[\mathcal{J}^\alpha_0 \mathcal{J}^\alpha_{12}\right] \equiv C^\alpha_{41}\left\langle \delta\mathcal{F}^2_\alpha \right\rangle_c^3 \left\langle \delta\mathcal{F}_\alpha(\hat{\Omega}_1)\delta\mathcal{F}_\alpha(\hat{\Omega}_2) \right\rangle_c; \tag{30}$$

$$\left\langle \delta\mathcal{F}^3_\alpha(\hat{\Omega}_1)\delta\mathcal{F}^2_\alpha(\hat{\Omega}_2) \right\rangle_c = (12S_a + 6S_b)\mathcal{C}_5\left[(\mathcal{J}^\alpha_0)^3 \mathcal{J}^\alpha_{12}\right] = C^\eta_{32}\mathcal{C}_5\left[(\mathcal{J}^\alpha_0)^3 \mathcal{J}^\alpha_{12}\right] \equiv C^\alpha_{32}\left\langle \delta\mathcal{F}^2_\alpha \right\rangle_c^3 \left\langle \delta\mathcal{F}_\alpha(\hat{\Omega}_1)\delta\mathcal{F}_\alpha(\hat{\Omega}_2) \right\rangle_c. \tag{31}$$

The expressions for the cumulant correlators given above apply in the large separation limit, that is, $\langle \delta\mathcal{F}_\alpha(\hat{\Omega}_1)\delta\mathcal{F}_\alpha(\hat{\Omega}_2)\rangle \ll \langle [\delta\mathcal{F}_\alpha(\hat{\Omega})]^2\rangle$. Although higher-order correction terms can be computed using the framework of the hierarchical ansatz, in practice the large separation limit is reached very quickly, even for nearby lines of sight. A detailed discussion of the tree amplitudes can be found in Munshi et al. (2000). In general, the cumulant correlators can be expressed as

$$\left\langle \delta\mathcal{F}^p_\alpha(\hat{\Omega}_1)\delta\mathcal{F}^q_\alpha(\hat{\Omega}_2) \right\rangle_c \equiv C^\eta_{pq}\mathcal{C}_{p+q}\left\{ \left[\mathcal{J}^\alpha_0(r)\right]^{p+q-2} \mathcal{J}^\alpha_{12}(r) \right\} = C^\alpha_{pq}\left\langle \delta\mathcal{F}^2_\alpha \right\rangle_c^{p+q-2} \langle \delta\mathcal{F}_\alpha(\hat{\Omega}_1)\delta\mathcal{F}_\alpha(\hat{\Omega}_2)\rangle_c. \tag{32}$$

Using these expressions, we can construct the joint 2PDF or the bias. To do so, we introduce the generating function $\beta^{(2)}_\alpha(y_1, y_2)$ for the normalized cumulant correlators:

$$\beta^{(2)}_\alpha(y_1, y_2) = \sum_{p,q}^{\infty} \frac{y_1^p y_2^q}{p!q!} C^\alpha_{pq} = \sum_{p,q}^{\infty} \frac{1}{p!q!} \frac{y_1^p y_2^q}{\langle \delta\mathcal{F}^2_\alpha \rangle_c^{p+q-2}} \frac{\langle \delta\mathcal{F}_\alpha(\hat{\Omega}_1)^p \delta\mathcal{F}_\alpha(\hat{\Omega}_2)^q \rangle_c}{\langle \delta\mathcal{F}_\alpha(\hat{\Omega}_1)\delta\mathcal{F}_\alpha(\hat{\Omega}_2)\rangle_c}. \tag{33}$$

Using equation (32), derived using the stellar model, we can make further progress:

$$\beta^{(2)}_\alpha(y_1, y_2) = \sum_{p,q}^{\infty} \frac{C^\alpha_{pq}}{p!q!} \frac{y_1^p}{\langle \delta\mathcal{F}^2_\alpha \rangle_c^{p-1}} \frac{y_2^q}{\langle \delta\mathcal{F}^2_\alpha \rangle_c^{q-1}} \frac{1}{\xi^{12}_\alpha} \int_0^{r_s} \mathrm{d}r\, d_\mathrm{A}^2(r) \frac{\omega^p_\alpha(r)\omega^q_\alpha(r)}{d_\mathrm{A}(r)^{2p} d_\mathrm{A}(r)^{2q}} [\mathcal{J}^\alpha_0(r)]^{p+q-1} \mathcal{J}^\alpha_{12}(r). \tag{34}$$

Next, we introduce the generating function $\beta^{(1)}_\alpha(y)$ for the normalized cumulant correlators. While $\beta^{(2)}_\alpha(y_1, y_2)$ is associated with C_{pq}, the generating function $\beta^{(1)}_\alpha(y)$ is the generating function for C_{p1} In three dimensions, the hierarchical ansatz ensures the factorization property $C_{pq} = C_{p1}C_{q1}$:

$$\beta^{(2)}_\alpha(y_1, y_2) = \int_{r_i}^{r_q} \mathrm{d}r\, w^2_\alpha(r)\, d_\mathrm{A}^2(r)\, \frac{\mathcal{J}^\alpha_{12}}{\xi^{12}_\alpha} \frac{\langle \delta\mathcal{F}^2_\alpha \rangle_c}{\mathcal{J}^\alpha_0(r)} \beta_\alpha \left[\frac{y_1}{\langle \delta\mathcal{F}^2_\alpha \rangle_c} \frac{\omega_\alpha(r)}{d_\mathrm{A}^2(r)} \mathcal{J}^\alpha_0(r) \right] \frac{\langle \delta\mathcal{F}^2_\alpha \rangle_c}{\mathcal{J}^\alpha_0(r)} \beta^{(1)}_\alpha \left[\frac{y_2}{\langle \delta\mathcal{F}^2_\alpha \rangle_c} \frac{\omega_\alpha(r)}{d_\mathrm{A}^2(r)} \mathcal{J}^\alpha_0(r) \right];$$

$$\beta^{(1)}_\alpha(y) = \sum_{p=1}^{\infty} \frac{C^\alpha_{p1}}{p!} y^p. \tag{35}$$

In terms of the reduced flux η, the generating function for the joint cumulant correlator can be written as

$$\begin{aligned} \beta^{(2)}_\eta(y_1, y_2) = \int_{r_i}^{r_q} \mathrm{d}r\, & \frac{d_\mathrm{A}^2(r)}{\left|\delta\mathcal{F}^{\min}_\alpha\right|^2} \frac{\mathcal{J}^\alpha_{12}(r)}{\xi^{12}_\alpha} \frac{\langle \delta\mathcal{F}^2_\alpha \rangle_c}{\mathcal{J}^\alpha_0(r)} \beta^{(1)}_\eta \left[\frac{y_1}{\langle \delta\mathcal{F}^2_\alpha \rangle_c} \frac{\omega_\alpha(r)}{d_\mathrm{A}^2(r)} \mathcal{J}^\alpha_0(r) \left|\delta\mathcal{F}^{\min}_\alpha\right| \right] \frac{\langle \delta\mathcal{F}^2_\alpha \rangle_c}{\mathcal{J}^\alpha_0(r)} \beta^{(1)}_\alpha \\ & \times \left[\frac{y_2}{\langle \delta\mathcal{F}^2_\alpha \rangle_c} \frac{\omega_\alpha(r)}{d_\mathrm{A}^2(r)} \mathcal{J}^\alpha_0(r) \left|\delta\mathcal{F}^{\min}_\alpha\right| \right]. \end{aligned} \tag{36}$$

These equations depend on the stellar model for the higher-order correlation functions. To simplify further, we replace the relevant integrals by the following approximate results:

$$\bar{\xi}_\alpha \approx \frac{1}{2}\Delta r \frac{\omega^2_\alpha(r_c)}{d^2_\mathrm{A}(r_c)} \left\{ \int \frac{\mathrm{d}^2 l}{(2\pi)^2} \mathrm{P}_\delta \left[\frac{l}{d_\mathrm{A}(r_c)} \right] \right\}; \qquad \xi^{12}_\alpha \approx \frac{1}{2}\Delta r \frac{\omega^2_\alpha(r_c)}{d^2_\mathrm{A}(r_c)} \left\{ \int \frac{\mathrm{d}^2 l}{(2\pi)^2} \mathrm{P}_\delta \left[\frac{l}{d_\mathrm{A}(r)} \right] \exp(\mathrm{i}\, \boldsymbol{l} \cdot \theta_{12}) \right\}; \tag{37}$$

$\Delta r = r_q - r_i$.

This leads to the following expression, which also preserves the factorization properties for the generating functions:

$$\beta^{(2)}_\eta(y_1, y_2) = \beta^{(1)}_\eta(y_1)\beta^{(1)}_\eta(y_2). \tag{38}$$

From the generating function $\beta^{(1)}_\eta(y)$, it is possible to construct the scaling function $b_\eta(x)$ that encodes all the information about the bias $b(\eta)$. The functions $b_\eta(x)$ can be recovered using the following integrals in the complex y plane (Balian & Schaeffer 1989):

$$b_\eta(x)h_\eta(x) = -\frac{1}{2\pi\mathrm{i}} \int_{-\mathrm{i}\infty}^{\mathrm{i}\infty} \mathrm{d}y \beta^{(1)}_\eta(y) \exp(xy); \qquad b_\eta(>x)h_\eta(>x) = -\frac{1}{2\pi\mathrm{i}} \int_{-\mathrm{i}\infty}^{\mathrm{i}\infty} \mathrm{d}y \frac{\beta^{(1)}_\eta(y)}{y} \exp(xy). \tag{39}$$

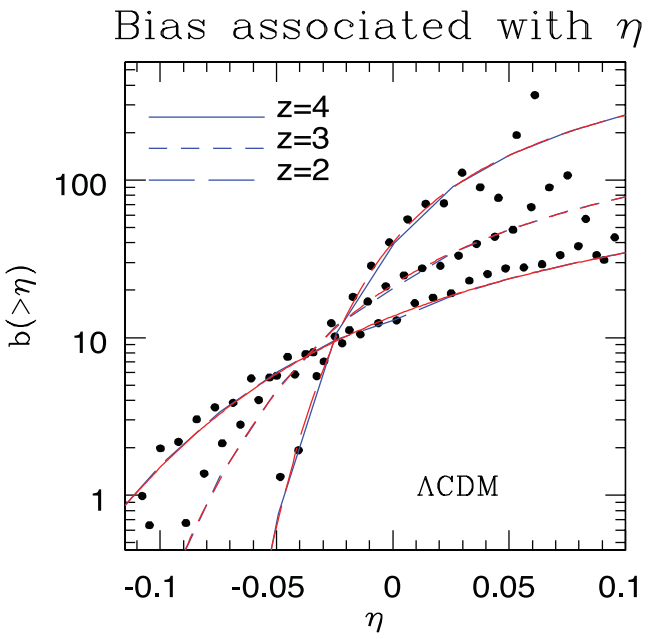

Figure 8. The cumulative bias $b(>\delta\mathcal{F}_\alpha)$ of the flux is plotted as a function of the flux. The lognormal distribution and the hierarchical ansatz generate nearly identical results. For a given positive δF_α, the bias is typically higher for a higher redshift. The bias $b(>\delta\mathcal{F}_\alpha)$ samples the underlying 3D bias associated with $\bar{\delta}$ [i.e. b($\bar{\delta}$)].

In addition to the usual scaling functions $h(x)$ and $b(x)$, which are associated with the scaling properties of PDF $p(\eta)$ and bias $b(\eta)$, we also include their cumulative versions $h(>x)$ and $b(>x)$, which are linked to $p(>\delta)$ and $b(>\delta)$ (i.e. the PDF and bias beyond a threshold δ). Using the hierarchical ansatz, we can write the 2PDF using the following factorized form:

$$p(\eta_1,\eta_2) = p(\eta_1)p(\eta_2)\left[1 + b(\eta_1)\xi_{12}^{\eta}b(\eta_2)\right]\,\mathrm{d}\eta_1\,\mathrm{d}\eta_2. \tag{40}$$

Finally, using the definition of η, we can also write the 2PDF of the flux decrement $\delta\mathcal{F}_\alpha$ for two different neighbouring lines of sight:

$$p_\alpha\left[\delta\mathcal{F}_\alpha(\Omega_1),\delta\mathcal{F}_\alpha(\Omega_2)\right] = p_\alpha\left[\delta\mathcal{F}_\alpha(\Omega_1)\right]p_\alpha\left[\delta\mathcal{F}_\alpha(\Omega_2)\right]\left\{1 + b_\alpha\left[\delta\mathcal{F}_\alpha(\Omega_1)\right]\xi_{12}^{\alpha}b_\alpha\left[\delta\mathcal{F}_\alpha(\Omega_2)\right]\right\}\,\mathrm{d}\delta\mathcal{F}_\alpha(\Omega_1)\,\mathrm{d}\delta\mathcal{F}_\alpha(\Omega_2). \tag{41}$$

The bias b_α for flux decrement and the bias associated with the underlying mass distribution η are related by the following expression:

$$b_\alpha(\delta\mathcal{F}_\alpha) = b_\eta(\eta)/|\delta\mathcal{F}_\alpha^{\min}|. \tag{42}$$

This approximate result also means that we can write $C_{p1}^{\alpha} = C_{p1}^{\eta}/|\delta\mathcal{F}_\alpha^{\min}|^{p-1}$; which implies that $C_{pq}^{\alpha} = C_{pq}^{\eta}/|\delta\mathcal{F}_\alpha^{\min}|^{p+q-2}$. Together, equations (25) and (42) are sufficient to model the one- and two-point distributions of transmitted flux. The fact that the final results are completely independent of specific models for the PDF of underlying density contrast indicates their general validity; we can use both the hierarchical model as well as the lognormal distribution as a model for the underlying density contrast $\delta(\boldsymbol{x}) = \eta(\boldsymbol{x}) - 1$.

Although we have only provided the joint PDF of two line-of-sight directions in this paper, the formalism can be extended to tackle an arbitrary number of lines of sight. The statistics derived using multiple lines of sight are directly linked to the statistics of hotspots in flux-decrement maps. It is interesting to note that the bias $b(x)$ introduced here has also been used in previous studies that have dealt with clustering of Lyman α absorbers. In a more general context, the correlation function of two overdense objects $\hat{\xi}_{12}$ can be expressed in terms of the underlying correlation function as $\hat{\xi}_{12}(r_1,r_2;x_1,x_2) = b(x_1)b(x_2)\xi_{12}(r_1,r_2)$, where the scaling parameters x_1 and x_2 are the scaling parameters associated with collapsed objects. This is a generic outcome of any hierarchical formalism and it has been used successfully to compute the bias associated with collapsed objects from clusters and groups to galactic-sized haloes (Valageas & Schaeffer 2000a). As is the case for the scaling function $h(x)$, we quote two asymptotes for the bias function $b(x)$ given by Bernardeau & Schaeffer (1992): (i) for $x \ll 1$, $b(x) \propto x^{(1-\omega)/2}$; (ii) for $x \gg 1$, $b(x) \propto x$. A more detailed discussion is given in Appendix A. The bias function $b(x)$ is independent of scale, as is the case for the scaled PDF $h(x)$. Information regarding a specific scale can be extracted by evaluating the scaling variable x for that scale.

We note that the lognormal model (see Appendix B) does not belong to the class of other scale-invariant or scaling models. However, the joint PDF can also be accurately computed using the lognormal model, and in the large separation limit the lognormal model can also be employed to compute the integrated bias.

The computation of the 2PDF or, equivalently, the bias was performed using a 512^2 grid. We computed the number of lines of sight where the flux decrement crosses a given threshold, which gives us the quantity $\int_{\delta_0}^{\infty}\int_{\delta_0}^{\infty} p(\delta_1,\delta_2)\mathrm{d}\delta_1\mathrm{d}\delta_2$. We also use the fractions of lines of sight where $\delta\mathcal{F}_\alpha$ crosses a threshold to compute $\int_{\delta_0}^{\infty} p(\delta)\mathrm{d}\delta$. Next, using the expression given in equation (7), we compute the resulting bias, which is presented in Fig. 8.

6 CONCLUSIONS

The diffuse IGM acts as a significant reservoir of baryons at low to intermediate redshift ($z < 5$), and it can be probed via the absorption lines in the spectrum of distant QSOs. The Lyman α absorption lines along the lines of sight are the result of a vast range of completely different classes of object. These objects include underdense neutral hydrogen clouds, haloes of large and overdense systems, which might have already reached virial equilibrium, as well as UV-heated systems that are strongly coupled to their environments. Previous studies have mainly dealt with the problem of the detailed modelling of a number of these objects as a function of their clustering and internal properties. Using self-consistent scaling models, which have a long history and were initially employed in galaxy clustering statistics, several authors have computed the column density distribution of Lyman α absorption systems, not only for the low column density Lyman α forest systems but also for Lyman limit systems and damped absorption systems. In addition to the hierarchical modelling, lognormal approximation is also quite successful in reproducing the clustering statistics of Lyman α absorption lines. In this paper, we have shown that the approaches using the lognormal approximation and the hierarchical ansatz generate nearly identical results. While previous studies focused only on one-point statistics, we have extended these results to two-point distributions and their lower-order moments.

In addition to the statistics of absorption lines, the statistics of the transmitted flux play an important complementary role in Lyman α studies. The flux can be treated as a continuous field. Various statistics that are often employed in analysing the flux include the line-of-sight power spectrum measurements, the estimation of the bispectrum and, more recently, the entire PDF. The flux PDF contains the information regarding cumulants to an arbitrary order. Clearly, the flux statistics and the column density distributions are related. One major goal in this study was to unify these two pictures in the context of the hierarchical ansatz or scaling models as well as the lognormal approximation.

The hierarchical model is primarily valid at smaller scales where the correlation function assumes a hierarchical form. Gravitational clustering is known to develop such a form of hierarchy, both in the perturbative (quasi-linear) regime as well as in the highly non-linear regime. The hierarchical ansatz can be used to describe the mass functions and the bias associated with collapsed objects using the scaling functions $h(x)$ and $b(x)$; the variable x is a scaling variable. Previous studies that have employed the hierarchical ansatz have shown that the column density distribution of absorption systems can be described using the same functional form for $h(x)$ and $b(x)$, which are often used for wide-ranging studies from galaxy clustering to thermal Sunyaev–Zel'dovich effects or the X-ray luminosity of clusters of galaxies. We have shown that the same analytical framework can also be used to understand the statistics of QSO flux measurements, thereby providing a unified statistical approach to what, at first sight, appear to be very different observables.

We have approached the modelling of the flux PDF in two different ways. For the 3D analysis, the PDF of the neutral hydrogen density contrast $\hat{\delta}$ is modelled according to the hierarchical ansatz as well as lognormal distribution. We find very good agreement with the numerical simulations for the entire range of redshifts that we have considered. The predictions from both these models are almost identical and differ only marginally in the less interesting underdense regions. We have also employed a modified version of the scale-invariant hierarchical approximation, which was developed recently (Valageas & Munshi 2004). This particular approximation provides a very accurate model for the clustering of $\hat{\delta}$. Using the fluctuating Gunn–Peterson approximation, we have mapped the $\hat{\delta}$ PDF to that of the transmitted flux F_α. We have found a reasonable approximation for the allowed range of parameters $A(z)$ and β that define the Gunn–Peterson approximation. Next, we considered the projected or the 2D distribution of flux. For projected statistics, we started by linking the cumulants and cumulant correlators for the flux and the underlying neutral hydrogen density contrast $\hat{\delta}$. Then, $\hat{\delta}$ has been taken to be a tracer of the underlying density contrast δ, modelled statistically using the hierarchical ansatz. Under certain simplifying assumptions, we have shown that the PDF of δ and the PDF of a suitably defined reduced flux decrement are linked through a very simple relation. Tests against numerical simulations show good agreement. The results were obtained for the entire bias functions that act as a generating function for the cumulant correlators. The scaling function $h(x)$ and the bias function $b(x)$ are also known to describe the number density and bias of overdense objects, respectively.

The formalism developed here can also be used to probe the higher-order cross-correlation statistics involving Lyman α flux decrement and the weak lensing convergence of CMB maps or those extracted from convergence maps constructed using the weak gravitational lensing of optical galaxies.

The Lyman α forest flux PDF has already been used to derive cosmological and astrophysical constraints (Viel, Bolton & Haehnelt 2009b). The continuum fitting of the QSO spectra, which is one of the main systematics, is taken into account in a conservative way in the interpretation of the data sets in such studies. The constraints were shown to be consistent with the *Wilkinson Microwave Anisotropy Probe* (*WMAP*) estimates. The error bars from a joint PDF and power-spectrum analysis were twice the size of those from *WMAP* alone. The first analyses used mainly UVES/VLT data, but the situation could improve now the data from SDSS-III are publicly available. The PDF we have discussed is constructed using models of gravitational clustering. However, the PDF is also sensitive to cosmological reionization, pre-heating and non-zero primordial non-Gaussianity. Such effects will leave distinct signatures in the flux PDFs, which will show up as a departure from the theoretical PDF that we have constructed, and hence they can be studied using the PDF as a tool. The bispectrum of Lyman α has been measured but not quantitatively interpreted nor combined with the power spectrum (e.g. Viel et al. 2004a). The flux PDF has instead been combined with the flux power and with wavelet analysis to obtain tighter constraints on cosmological and astrophysical parameters. Indeed, it is true that the bispectrum has inbuilt shape dependence information. However, the PDFs that we study are sensitive to non-Gaussianity even at a level higher than the bispectrum. A quantitative estimate of gain in signal-to-noise in pinpointing the cosmological parameters, taking into account the entire PDF, will be presented elsewhere using the formalism developed by Valageas, Munshi & Barber (2005).

ACKNOWLEDGMENTS

DM and PC acknowledge support from STFC standard grant ST/G002231/1 at the School of Physics and Astronomy at Cardiff University, where this work was completed. MV acknowledges support from ASI/AAE, INFN PD-51, PRIN INAF, PRIN MIUR grants and from the ERC-FP7 Starting Grant 'cosmoIGM'. We would like to thank Alan Heavens, Patrick Valageas, Ludo van Waerbeke and Martin White for many useful discussions. We thank Tirthankar Roy Choudhury for his input. DM would also like to thank Francis Bernardeau for making a copy of his code available to us, which we have modified to compute the PDF and bias of the Lyman α flux for the perturbative model. It is a pleasure for DM to thank Patrick Valageas for sharing codes that were used for this study. We also thank an anonymous referee for many constructive comments that have helped to improve this paper.

REFERENCES

Balian R., Schaeffer R., 1989, A&A, 220, 1
Barber A. J., Munshi D., Valageas P., 2004, MNRAS, 347, 667
Bernardeau F., 1992, ApJ, 392, 1
Bernardeau F., 1994, A&A, 291, 697
Bernardeau F., Schaeffer R., 1992, A&A, 255, 1
Bernardeau F., Schaeffer R., 1999, A&A, 349, 697
Bernardeau F., Valageas P., 2000, A&A, 364, 1
Bernardeau F., Colombi S., Gaztanaga E., Scoccimarro R., 2002, Phys. Rep., 367, 1
Bi H., 1993, ApJ, 405, 479
Bi H., Davidson A. F., 1997, ApJ, 479, 523
Bolton J. S., Haehnelt M. G., Viel M., Springle V., 2005, MNRAS, 357, 1178
Bolton J. S., Viel M., Kim T-S., Haehnelt M. G., Carswell R. F., 2008, MNRAS, 386, 1131
Bolton J. S., Oh S. P., Furlanetto S. R., 2009, MNRAS, 396, 2405
Bouchet F., Strauss M. A., Davis M., Fisher K. B., Yahil A., Huchra J. P., 1993, ApJ, 417, 36
Cen R., Miralda Escudé J., Ostriker J. P., Rauch M., 1994, ApJ, 437, L83
Coles P., Jones B., 1991, MNRAS, 248, 1
Colombi S., 1994, ApJ, 435, L536
Coppolani F. et al., 2006, MNRAS, 370, 1804
Croft R. A. C., Weinberg D. H., Katz N., Hernquist L., 1998, ApJ, 495, 44
Croft R. A. C., Weinberg D. H., Pettini M., Hernquist L., Katz N., 1999, ApJ, 520, 1
Croft R. A. C., Weinberg D. H., Bolte M., Burles S., Hernquist L., Katz N., Kirkman D., Tytler D., 2002, ApJ, 581, 20
Davis M., Peebles P. J. E., 1977, ApJS, 34, 425
D'Odorico V., Petitjean P., Cristiani S., 2002, A&A, 390, 13
Doroshkevich A. G., Shandarin S. F., 1977, MNRAS, 179, 95
Eisenstein D. J., Hu W., 1998, ApJ, 496, 605
Eisenstein D. J. et al., 2011, AJ, 142, 72
Fry J. N., 1984, ApJ, 279, 499
Gnedin N. Y., Hui L., 1996, ApJ, 472, L73
Gnedin N. Y., Hui L., 1998, MNRAS, 296, 44
Groth E., Peebles P. J. E., 1977, ApJ, 217, 385
Guimarães R., Petitjean P., Rollinde E., de Carvalho R. R., Djorgovski S. G., Srianand R., Aghaee A., Castro S., 2007, MNRAS, 377, 657
Gunn J. E., Peterson B. A., 1965, ApJ, 142, 1633
Haardt F., Madau P., 1996, ApJ, 461, 20
Hamilton A. J. S., 1985, ApJ, 292, L35
Hui L., 1999, ApJ, 519, L9
Hui L., Gnedin N. Y., 1997, MNRAS, 292, 27
Hui L., Haiman Z., 2003, ApJ, 596, 9
Hui L., Gnedin N. Y., Zhang Y., 1997, MNRAS, 292, 27
Kaiser N., 1992, ApJ, 388, 272
Kayo I., Taruya A., Suto Y., 2001, ApJ, 561, 22
Kim T-S., Bolton J. S., Viel M., Haehnelt M. G., Carswell R. F., 2007, MNRAS, 382, 1657
Kofman L., Bertschinger E., Gelb J. M., Nusser A., Dekel A., 1994, ApJ, 420, 44
Lidz A., Heitmann K., Hui L., Habib S., Rauch M., Sargent W. L. W., 2006, ApJ, 638, 27
Limber D. N., 1954, ApJ, 119, 665
McDonald P., 2003, ApJ, 585, 34
McDonald P., Eisenstein D., 2007, Phys. Rev. D, 76, 063009
McDonald P., Miralda Escudé J., 1999, ApJ, 518, 24
McDonald P., Miralda Escudé J., Rauch M., Sargent W. L. W., Barlow T. A., Cen R., 2001, ApJ, 562, 52
McDonald P., Seljak U., Cen R., Bode P., Ostriker J. P., 2005, MNRAS, 360, 1471
McDonald P., Seljak U., Burles E. A., 2006, ApJS, 163, 80
McGill C., 1990, MNRAS, 242, 544
McQuinn M., Lidz A., Zaldariagga M., Hernquist L., Hopkins P. F., Dutta S., Faucher-Giguere C.-A., 2009, ApJ, 694, 842
Matarrese S., Mohayee R., 2002, MNRAS, 329, 37
Meiksin A., 2009, Rev. Mod. Phys., 81, 1405

Meiksin A., White M., 2001, MNRAS, 324, 141
Munshi D., Coles P., 2000, MNRAS, 313, 148
Munshi D., Heavens A., 2010, MNRAS, 401, 2406
Munshi D., Jain B., 2000, MNRAS, 318, 109
Munshi D., Jain B., 2001, MNRAS, 322, 107
Munshi D., Coles P., Melott A., 1999a, MNRAS, 310, 892
Munshi D., Coles P., Melott A., 1999b, MNRAS, 307, 387
Munshi D., Melott A., Coles P., 2000, MNRAS, 311, 149
Munshi D., Valageas P., van Waerbeke L., Heavens A., 2008, Phys. Rep., 462, 67
Munshi D., Joudaki S., Smidt J., Coles P., 2011, MNRAS, submitted (arXiv:1106.0766)
Peeples M. S., Weinberg D. H., Davé R., Fardal M. A., Katz N., 2010, MNRAS, 404, 1281
Rauch M. et al., 1997, ApJ, 489, 7
Rauch M., Becker G. D., Viel M., Sargent W. L. W., Smette A., Simcoe R. A., Barlow T. A., Haehnelt M. G., 2005, ApJ, 632, 58
Rollinde E., Pettijean P., Pichon C., Colombi S., Aracil B., D'Odorico V., Haehnelt M. G., 2003, MNRAS, 341, 1279
Ross N. P. et al., 2012, ApJS, 199, 3
Roy Choudhury T., Padmanabhan T., Srianand R., 2001, MNRAS, 322, 561
Saitta F., D'Odorico V., Bruscoli M., Cristiani S., Monaco P., Viel M., 2008, MNRAS, 385, 519
Schaye J., Theuns T., Leonard A., Efstathiou G., 1999, MNRAS, 310, 57
Seljak U., Slosar A., McDonald P., 2006, JCAP, 10, 14
Slosar A. et al., 2011, JCAP, 09, 001
Springel V., 2005, MNRAS, 364, 1105
Szapudi I., Szalay A. S., 1993, ApJ, 408, 43
Szapudi I., Szalay A. S., 1997, ApJ, 481, L1
Szapudi I., Szalay A. S., 1999, ApJ, 515, L43
Taruya A., Takada M., Hamana T., Kayo I., Futamase T., 2002, ApJ, 571, 638
Theuns T., Leonard A., Efstathiou G., Pearce F. R., Thomas P. A., 1998, MNRAS, 301, 478
Theuns T., Viel M., Kay S., Schaye J., Carswell R. F., Tzanavaris P., 2002a, ApJ, 578, L5
Theuns T., Schaye J., Zaroubi S., Kim T-S., Tzanavaris P., Carswell B., 2002b, ApJ, 567, L103
Tytler D. et al., 2004, ApJ, 617, 1
Valageas P., 2000, A&A, 354, 767
Valageas P., Munshi D., 2004, MNRAS, 354, 1146
Valageas P., Schaeffer R., 1999, A&A, 345, 329
Valageas P., Schaeffer R., 2000a, A&A, 356, 771
Valageas P., Schaeffer R., 2000b, A&A, 359, 821
Valageas P., Silk J., 1999, A&A, 347, 1
Valageas P., Schaeffer R., Silk J., 1999, A&A, 345, 691
Valageas P., Balbi A., Silk J., 2001a, A&A, 367, 1
Valageas P., Silk J., Schaeffer R., 2001b, A&A, 366, 363
Valageas P., Schaeffer R., Silk J., 2002, A&A, 388, 741
Valageas P., Munshi D., Barber A. J., 2005, MNRAS, 356, 386
Vallinotto A., Viel M., Das S., Spergel D. N., 2011, ApJ, 735, 38
Vallinotto A., Das S., Spergel D. N., Viel M., 2009, Phys. Rev. Lett., 103, 091304
Viel M., Haenelt M. G., 2006, MNRAS, 365, 231
Viel M., Matarrese S., Mo H. J., Haehnelt M. G., Thuns T., 2002, MNRAS, 329, 848
Viel M., Matarrese S., Heavens A., Haehnelt M. G., Kim T-S., Springel V., Hernquist L., 2004a, MNRAS, 347, L26
Viel M., Haenelt M. G., Springel V., 2004b, MNRAS, 354, 684
Viel M., Becker G. D., Bolton J. S., Haehnelt M. G., Rauch M., Sargent W. L. W., 2008, Phys. Rev. Lett., 100, 041304
Viel M., Branchini E., Dolag K., Grossi M., Matarrese S., Moscardini L., 2009a, MNRAS, 393, 774
Viel M., Bolton J. S., Haehnelt MG., 2009b, MNRAS, 399, L39
Zel'dovich Ya. B., 1970, A&A, 5, 84

APPENDIX A: HIERARCHICAL ANSATZ: A VERY BRIEF REVIEW

There is no complete analytical model for the evolution of gravitational clustering in the non-linear regime, and the Eulerian and Lagrangian perturbation theories (Bernardeau et al. 2002) are often used to describe clustering in the quasi-linear regime. The halo model is extensively used and is very successful in modelling fully evolved structure formation. A parallel approach depends on the hierarchical nature of the correlation functions that develop during the non-linear regime. This has a long history in describing clustering dark matter distribution as well as collapsed objects. Additional assumptions regarding virialization and hydrodynamical equilibrium can be used in association to make specific predictions regarding diverse cosmological phenomenon from the luminosity of X-ray clusters (Valageas & Schaeffer 2000b), the column density distribution of neutral hydrogen (Valageas, Schaeffer & Silk 2002), the redshift evolution bias (Valageas, Silk & Schaeffer 2001b), the mass and luminosity distribution of galaxies and clusters (Valageas & Schaeffer 1999), CMB secondaries, such as the thermal and kinetic Sunyaev–Zel'dovich effect (Valageas, Balbi & Silk 2001a; Munshi et al. 2011), and the reheating and reionization of the Universe (Valageas & Schaeffer 1999; Valageas & Silk 1999; Valageas et al. 2002). Weak lensing observables have already been studied in this framework (Valageas & Schaeffer 1999; Bernardeau & Valageas 2000; Munshi & Jain 2000, 2001; Valageas 2000).

The hierarchical ansatz (Balian & Schaeffer 1989) is remarkably successful at making approximate calculations of the entire PDF and bias of the density field, improving significantly upon the order-by-order analysis of other approaches (see Bernardeau et al. 2002 for a detailed review). The hierarchical ansatz in the highly non-linear regime depends on assuming a specific correlation hierarchy; however, in the quasi-linear regime, it can be linked to the gravitational dynamics using perturbative analysis.

A1 Highly non-linear regime

The PDF $p(\delta)$ and the bias $b(\delta)$ can both be constructed from knowledge of the VPF $\phi(y) = \sum_{p=1} S_p\, y^p/p!$ and its two-point analogue $\tau(y) = \sum_p C_{p1}\, y^p/p!$, where the parameters S_p and C_{p1} are normalized cumulants and cumulant correlators for the density field. The PDF is related to the scaling function $h(x)$ in the main body of the paper $p(\delta) = h(x)/\bar{\xi}_2^2$ with $x = (1+\delta)/\bar{\xi}_2$:

$$p(\delta) = \int_{-\mathrm{i}\infty}^{\mathrm{i}\infty} \frac{\mathrm{d}y}{2\pi\mathrm{i}} \exp\left[\frac{(1+\delta)y - \phi(y)}{\bar{\xi}_2}\right]; \qquad b(\delta)p(\delta) = \int_{-\mathrm{i}\infty}^{\mathrm{i}\infty} \frac{\mathrm{d}y}{2\pi\mathrm{i}} \tau(y) \exp\left[\frac{(1+\delta)y - \phi(y)}{\bar{\xi}_2}\right]. \tag{A1}$$

The modelling of $\phi(y)$ and $\tau(y)$ needs a detailed knowledge of the entire correlation hierarchy. The detailed knowledge of the entire correlation hierarchy is encoded in the vertex generating function $\mathcal{G}(\tau)$. Typically, for large values of y, the VPF exhibits a power law $\phi(y) = a y^{1-\omega}$. There are no theoretical estimates of ω and it is generally estimated from numerical simulations. The parameter typically takes a value $\omega = 0.3$ for CDM-like spectra. For small but negative values of y, the functions $\phi(y)$ and $\tau(y)$ develop a singularity in the complex plane, which is described by the following parametrization:

$$\phi(y) = \phi_s - a_s \Gamma(\omega_s)(y - y_s)^{-\omega_s}; \qquad \tau(y) = \tau_s - b_s (y - y_s)^{-\omega_s - 1}. \tag{A2}$$

The singularity structure of $\phi(y)$ and $\tau(y)$ depends on the nature of the vertex generating function $G(\tau)$ and its behaviour near the singularity τ_s:

$$a_s = \frac{1}{\Gamma(-1/2)} \mathcal{G}'(\tau_s)\mathcal{G}''(\tau_s) \left[\frac{2\mathcal{G}'(\tau_s)\mathcal{G}''(\tau_s)}{\mathcal{G}'''(\tau_s)}\right]^{3/2}; \qquad b_s = \left[\frac{2\mathcal{G}'(\tau_s)\mathcal{G}''(\tau_s)}{\mathcal{G}'''(\tau_s)}\right]^{1/2}. \tag{A3}$$

However, the parameters ω and a can be described in terms of a parameter y_s, which in turn describes the exponential decay of the PDF for large density contrast δ:

$$\omega = \frac{k_a}{k_a + 2}; \qquad a = \frac{k_a + 2}{2} k_a^{k_a/k_a + 2}; \qquad -\frac{1}{y_s} = x_\star = \frac{1}{k_a} \frac{(k_a+2)^{k_a+2}}{(k_a+1)^{k_a+1}}. \tag{A4}$$

Thus, the PDF and the bias have two distinct regimes that are dictated by the two asymptotes. For intermediate values of δ, the PDF shows a power-law behaviour. The PDF and the bias are given by the following expressions:

$$\bar{\xi}^{-[\omega/(1-\omega)]} \ll 1 + \delta \ll \bar{\xi}; \qquad p(\delta) = \frac{a}{\bar{\xi}_2^2} \frac{1-\omega}{\Gamma(\omega)} \left(\frac{1+\delta}{\xi_2}\right)^{\omega - 2}; \qquad b(\delta) = \left(\frac{\omega}{2a}\right)^{1/2} \frac{\Gamma(\omega)}{\Gamma[(1/2)(1+\omega)]} \left(\frac{1+\delta}{\bar{\xi}_2}\right)^{(1-\omega)/2}. \tag{A5}$$

For large values of δ, however, the PDF shows an exponential behaviour:

$$1 + \delta \gg \bar{\xi}_2; \qquad p(\delta) = \frac{a_s}{\bar{\xi}_2^2} \left(\frac{1+\delta}{\bar{\xi}_2}\right) \exp\left(-\frac{1+\delta}{x_\star \bar{\xi}_2}\right); \qquad b(\delta) = -\frac{1}{\mathcal{G}'(\tau_s)} \frac{(1+\delta)}{\bar{\xi}_2}. \tag{A6}$$

At very small values of δ, the PDF shows an exponential decay, which is described only by the parameter ω:

$$1 + \delta \ll \bar{\xi}_2; \qquad p(\delta) = a^{-1/(1-\omega)} \bar{\xi}_2^{\omega/(1-\omega)} \sqrt{\frac{(1-\omega)^{1/\omega}}{2\pi\omega z^{(1+\omega)/\omega}}} \exp\left[-\omega\left(\frac{z}{1-\omega}\right)^{-(1-\omega)/\omega}\right];$$

$$b(\delta) = -\left(\frac{2\omega}{\bar{\xi}_2}\right)^{1/2} \left(\frac{1-\omega}{z}\right)^{(1-\omega)/2\omega}. \tag{A7}$$

The range of δ for which the power-law regime is valid depends on the value of $\bar{\xi}_2$. For smaller values of $\bar{\xi}_2$, the power-law regime is less pronounced.

A2 Quasi-linear regime

In the quasi-linear regime, the parameters that describe the generating functions can be directly linked with gravitational dynamics (Bernardeau 1992, 1994). The PDF and bias in the intermediate power-law regime in the quasi-linear regime are given by the following result:

$$p(\delta)d\delta = \frac{1}{-\mathcal{G}'_\delta(\tau)} \left[\frac{1 - \tau\mathcal{G}''_\delta(\tau)/\mathcal{G}'_\delta(\tau)}{2\pi\bar{\xi}_2}\right]^{1/2} \exp\left(-\frac{\tau^2}{2\bar{\xi}_2}\right) \mathrm{d}\tau; \qquad b(\delta) = -\left(\frac{k_a}{\bar{\xi}_2}\right) \left\{[1 + \mathcal{G}_\delta(\tau)]^{1/k_a} - 1\right\}; \tag{A8}$$

$$\mathcal{G}_\delta(\tau) = \mathcal{G}(\tau) - 1 = \delta. \tag{A9}$$

For the large density contrast, the exponential decay takes the following form:

$$p(\delta)d\delta = \frac{3a_s\sqrt{\bar{\xi}_2}}{4\sqrt{\pi}} \delta^{-5/2} \exp\left(-|y_s|\frac{\delta}{\bar{\xi}_2} + \frac{|\phi_s|}{\bar{\xi}_2}\right) \mathrm{d}\delta; \qquad b(\delta) = -\frac{1}{\mathcal{G}'(\tau_s)} \frac{(1+\delta)}{\bar{\xi}_2}. \tag{A10}$$

These results ignore the loop corrections to tree-level perturbation theory, but take into account correlation hierarchy to an arbitrary order.

APPENDIX B: LOGNORMAL DISTRIBUTION

The evolution of the PDF $p(\delta)$ of density field δ due to gravitational clustering has been studied extensively in many cosmological contexts. The lognormal distribution (Hamilton 1985; Coles & Jones 1991; Bouchet et al. 1993; Kofman et al. 1994) is known to accurately reproduce the results from numerical simulations in the quasi-linear regime and has been used to model both one- and two-point PDFs. In general, the lognormal distribution can provide a good statistical description of a random variable if it can be modelled as a product of many other random variables (Colombi 1994; Kayo, Taruya & Suto 2001; Taruya et al. 2002):

$$p(\delta)\,\mathrm{d}\delta = \frac{1}{\sqrt{2\pi\Sigma}}\exp\left(-\frac{\Lambda^2}{2\Sigma}\right)\frac{\mathrm{d}\delta}{1+\delta}; \tag{B1}$$

$$\Sigma = \ln(1+\sigma^2); \qquad \Lambda = \ln\left[(1+\delta)\sqrt{(1+\sigma^2)}\right]; \tag{B2}$$

$$p(\delta_1,\delta_2)\,\mathrm{d}\delta_1\,\mathrm{d}\delta_2 = \frac{1}{2\pi\sqrt{\Sigma^2 - X_{12}^2}}\exp\left[-\frac{\Sigma(\Lambda_1^2+\Lambda_2^2) - 2X_{12}\Lambda_1\Lambda_2}{2(\Sigma^2 - X_{12}^2)}\right]\frac{\mathrm{d}\delta_1}{1+\delta_1}\frac{\mathrm{d}\delta_2}{1+\delta_2}; \tag{B3}$$

$$\Lambda_i = \ln\left[(1+\delta_i)\sqrt{(1+\sigma^2)}\right]; \qquad X_{12} = \ln(1+\xi_{12}). \tag{B4}$$

In the lowest order in ξ_{12}, the lognormal model takes a factorized form. In this limit, a bias function $b(\delta)$ can be defined:

$$p(\delta_1,\delta_2) = p(\delta_1)p(\delta_2)[1 + b(\delta_1)\xi_{12}b(\delta_2)]; \qquad b(\delta_i) = \Lambda_i/\Sigma. \tag{B5}$$

The lognormal distribution has also been used to model many cosmological observations from galaxy surveys to weak lensing data.

This paper has been typeset from a TEX/LATEX file prepared by the author.